2011

STEADY FLOW OF A THIN VISCOELASTIC JET

Moinuddin Ahmed

STEADY FLOW OF A THIN VISCOELASTIC JET

(Spine title: Steady Flow of a Thin Viscoelastic Jet)

(Thesis format: Monograph)

By

Moinuddin Ahmed

Graduate Program in Faculty of Engineering
Department of Mechanical & Materials Engineering

A thesis submitted in partial fulfillment
of the requirements for the degree of
Master of Engineering Science

School of Graduate and Postdoctoral Studies
The University of Western Ontario
London, Ontario, Canada

THE UNIVERSITY OF WESTERN ONTARIO
SCHOOL OF GRADUATE AND POSTDOCTORAL STUDIES

CERTIFICATE OF EXAMINATION

Supervisor

Prof. Roger E. Khayat

Examiners

Prof. Andrew N. Hrymak

Prof. Chao Zhang

Prof. Eric Savory

The thesis by

Moinuddin Ahmed

entitled:

Steady Flow of a Thin Viscoelastic Jet

is accepted in partial fulfilment of the
requirements for the degree of
Master of Engineering Science

Date_____

_____
Chair of the Thesis Examination Board

ABSTRACT

The symmetric two-dimensional flow of a thin viscoelastic fluid jet emerging from a vertical channel is examined theoretically in this study. The fluid is assumed to be a polymeric solution, modeled following the Oldroyd-B constitutive equation. The influence of inertia, elasticity and gravity in the presence of surface tension is investigated for steady flow only. Special emphasis is placed on the initial stages of jet development. The viscoelastic boundary-layer equations are solved by expanding the flow field in terms of orthonormal shape functions. In contrast to the commonly used depth-averaging technique, the proposed method predicts the shape of the free surface, as well as the velocity and stress components within the fluid. It was found that the jet reaches the same uniform thickness regardless of Reynolds number in the absence of gravity. However, the distance to reach the uniform thickness depends on inertia. Presence of gravity enhances the jet contraction and leads to possible jet break up. Presence of surface tension tends to prohibit the contraction and flatten the jet surface. In contrast to the Newtonian flow, viscoelastic flow displays uniform flow much farther from the channel exit. Swelling is observed as Deborah number increases. The velocity and stress components profiles suggest that elasticity tends to play different role to inertia. Surface tension tends to flatten the jet surface similar to the Newtonian jet, but the stress components are not affected much in the case of a viscoelastic jet. The numerical solution is validated with experiment and good qualitative agreement is achieved.

Keywords: Viscoelastic fluid, polymer, planar, Oldroyd-B, thin jet, inertia, elasticity, surface tension, spectral method, Tanner's theory, boundary layer, extrudate swell.

CO-AUTHORSHIP

The following thesis contains materials from the manuscript that has been accepted for publication in "Journal of Applied Numerical Mathematics" and co-authored by Moinuddin Ahmed[1], Dr. Roger E. Khayat[1] and Michael A. Hanyk[1].

[1] Department of Mechanical and Materials Engineering
The University of Western Ontario
London, Ontario, Canada.

ACKNOWLEDGEMENTS

The author gratefully acknowledges his advisor Professor Roger E. Khayat for his invaluable support and guidance and consistent encouragement throughout the course of this work.

The author is thankful to his co-workers and friends from the *Fluid Mechanics and Polymer Processing Research Laboratory* for their helpful discussions and for creating a friendly and enjoyable working atmosphere.

The financial support of the Natural Sciences and Engineering Research Council of Canada (NSERC) and of the University of Western Ontario is acknowledged.

The author is deeply indebted to his parents for their moral support, sacrifice and encouragement.

TABLE OF CONTENTS

LIST OF FIGURES

LIST OF APPENDICES

NOMENCLATURE

a	Solute to solution viscosity ratio
A	Orthonormal shape function for streamwise velocity component
B	Orthonormal shape function for normal stress component
C	Orthonormal shape function for transverse stress component
Ca	Capillary number
D	Orthonormal shape function for shear stress component
De	Deborah number
Fr	Froude number
g	Gravitational acceleration
G	Gravity number
h	Film height (Dimensionless)
H_0	Reference length (transverse direction)
L	Reference length (streamwise direction)
M	Number of modes
n_x, n_z	Components of the normal vector in x and z direction.
N_1	Primary normal stress difference
N_2	Secondary normal stress difference
N-S	Navier-Stokes equation
O	Order of
p	Pressure (dimensionless)
P	Hydrostatic pressure
q	Streamwise normal stress (dimensionless)
Q_i	Streamwise normal stress expansion coefficient (x, t)
r	Transverse normal stress (dimensionless)
R_i	Transverse normal stress expansion coefficient (x, t)
Re	Reynolds number
Rv	Solvent to solute viscosity ratio
s	Shear stress (dimensionless)

S_i	Shear stress expansion coefficient (x, t)
t	Time (dimensionless)
t_X	Traction force component in x direction
t_Z	Traction force component in z direction
T_{XX}	Streamwise normal stress
T_{ZZ}	Transverse normal stress
T_{XZ}	Shear stress
u	Streamwise velocity component (dimensionless)
U_0	Mean velocity
U_i	Streamwise velocity expansion coefficient (x, t)
w	Transverse velocity component(dimensionless)
We	Weber number
x	x-axis position vector (dimensionless)
X	x-axis position vector
z	z-axis position vector (dimensionless)
Z	z-axis position vector
α, β, γ	Constants
δ	Kronecker delta
∇	Gradient operator
ε	Perturbation parameter
λ	Relaxation time
μ	Solution viscosity
μ_s	Newtonian solvent viscosity
μ_p	Polymeric solute viscosity
ξ	Transformation – z-axis (x, z, t)
ρ	Fluid density
Σ	Sum of viscous and polymeric stress tensor
τ	Transformation – time (x, z, t)
χ	Transformation – x-axis (x, z, t)
$\langle\rangle$	Integration over the interval $\xi \in [0, 1]$

CHAPTER 1

INTRODUCTION

1.1 General introduction

Thin-film flow is encountered as a fundamental fluid dynamics problem in various realistic settings such as extrusion, coating, lubrication, flow of lava etc. The thin film flows with free surface display a variety of interesting dynamics, since the boundary is deformable. In this case, free surface flow problems are challenging because the flow domain is unknown, and the unknown free surface must be determined as part of the problem. This is in sharp contrast to most fluid mechanics problems where the flow domain and boundaries are known. Thus, for a free surface flow problem, both the flow field and the free surface shape must be determined in space and time. The reason for studying these flows is to gain understanding of a great range of phenomena, which in turn allows making predictions in areas of practical importance.

The study of vertical liquid jets is of interest in connection with spinning, coating, film casting and rheological measurements of extension characteristics (Tanner 2000, Middleman 1977, Osswald & Hernandez-Ortiz 2006, Agassant et al. 1986). Due to the presence of solid boundaries, stresses are built up inside the channel. But as the fluid emerges from the channel into the air, the viscous shear stress is eliminated at the newly formed surface. Experimental observations suggest that the flow just outside of the channel can experience an expansion or contraction depending on the Reynolds number (Goren and Wronski 1966).

Polymeric fluids exhibit different behavior from the Newtonian fluid. The governing equations for any fluid consist of field equations resulting from the conservation laws and constitutive equations. But the constitutive equations, which relate the stress to the motion of the continuum, vary from one fluid to another. Newton's viscosity law cannot

be applied to describe polymeric fluids. Since there is no universal constitutive law for viscoelastic fluids, different constitutive models often lead to different flow patterns.

In general, the solution of film flow for a Newtonian fluid requires solving the Navier-Stokes equations. For a viscoelastic fluid, the conservation equations are solved together with the stress equations. The constitutive law for stress in this case depends on the type of flow problem. More precisely, the choice of a suitable constitutive equation depends on whether the flow is shear or elongation dominated. Elongational flow differs from shear flow in that the velocity gradient lies along the flow direction. In uni or biaxial extension, unlike shear, the principle strain direction is parallel to the direction of the extension, so that no rotation of the fluid is induced. Elongational flow is thus irrotational (Robert & Gregory 1994).

The presence of non-Newtonian effects in a fluid is expected to alter the flow characteristics. In elongational flow such as fiber spinning and film casting, experimental observations indicate that there are qualitative differences in the velocity, fiber diameter/film thickness and marginal stability conditions (Chang & Denn 1979).

The present theoretical study is focused on the planar flow of an incompressible polymeric jet emerging from a vertical channel. The jet is assumed to be thin. The emphasis will be on pressure-driven flow. Special emphasis is placed on the jet development as it emerges from the channel. Only steady state flow is considered in this thesis. The influence of elasticity, inertia and gravity on the shape of the free surface, the profiles of velocity and stress is explored. In contrast to existing theoretical studies, surface tension effect has not been neglected.

1.2 Relevance to reality

The present work is of fundamental importance given the significant qualitative role that elasticity plays in this case. In general, inertia has been neglected in most of the studies on viscoelastic jets. This can be quite reasonably justified, since in most practical applications of polymeric liquids, inertia is effectively small. However, there are still

applications such as fiber spinning, film casting and high-speed extrusion in which inertia plays a significant role. Inertia becomes particularly important in modern high-speed film casting. Experiments on film casting and fiber spinning (Doufas & McHugh 2001; Seyfzadeh, Harrison & Carlson 2005) also suggest that inertia has a significant effect on the stability region of these processes.

The viscosity of polymeric fluids can vary from 10^2 to 10^6 Pa s (Bird et al. 1987). Thus, in commercial fiber spinning and film casting processes (depending on the type of the polymer), the Reynolds number may have a wide range of values. For example, the Reynolds number of a Newtonian fiber spinning process in the experiment performed by Donnelly and Weinberger (1975) was reported to be less than 0.68×10^{-3}. However, more recently, Doufas et al. (2000) carried out their simulation by using the data from the spinning of Nylon 66. They estimated the Reynolds number in this case to be in the range 4.09 to 9.81. Some examples of the product of extrusion, fiber spinning and film casting processes are pipe/tubing, weather stripping, fence, deck railing, window frames, adhesive tape, film sheets, threads and wire insulation. Thus, the present work will help optimize the polymer process and product design by elucidating the range of optimal fluid parameters and flow conditions.

Fiber spinning is the process in which a cylindrical liquid thread of molten polymer is continuously extruded vertically through a spinneret, a die with multiple orifices. After initially swelling (a phenomenon called die swell), the thread is drawn down to a smaller diameter by an axial force. The process is schematically depicted in figure 1.1.

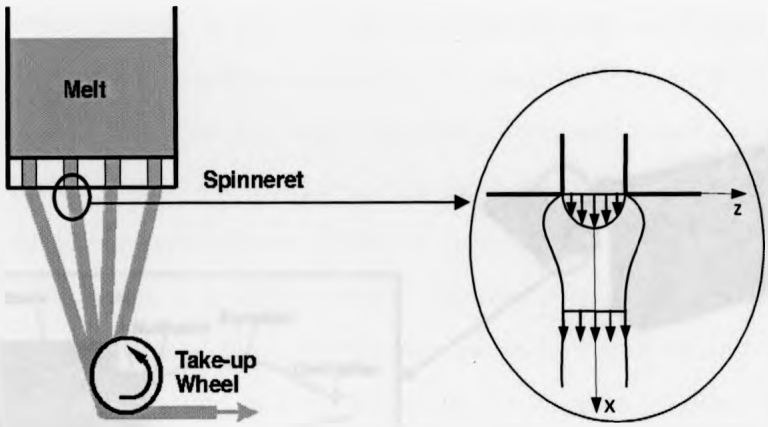

Figure 1.1 Schematic of the fiber spinning process. The molten polymers are extrudate through an orifice or die. After die swell, the thread is drawn down to a smaller diameter by an axial force (part of figure taken from www.polymerprocessing.com).

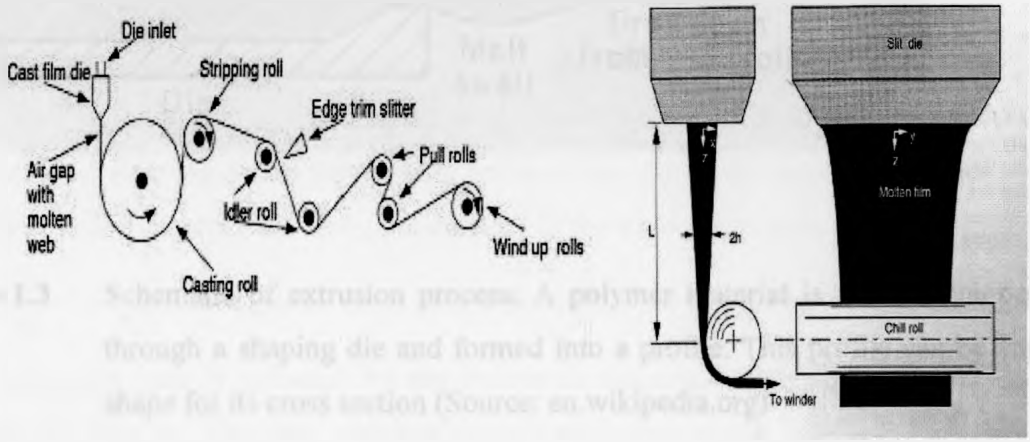

Figure 1.2 Schematic of a typical film casting process. Thin film is extruded through a slit die onto a chilled roll where it is quenched. After passing through a system of rollers, the film is wound onto a roll (figure taken from Osswald & Hernandez-Ortiz 2006)

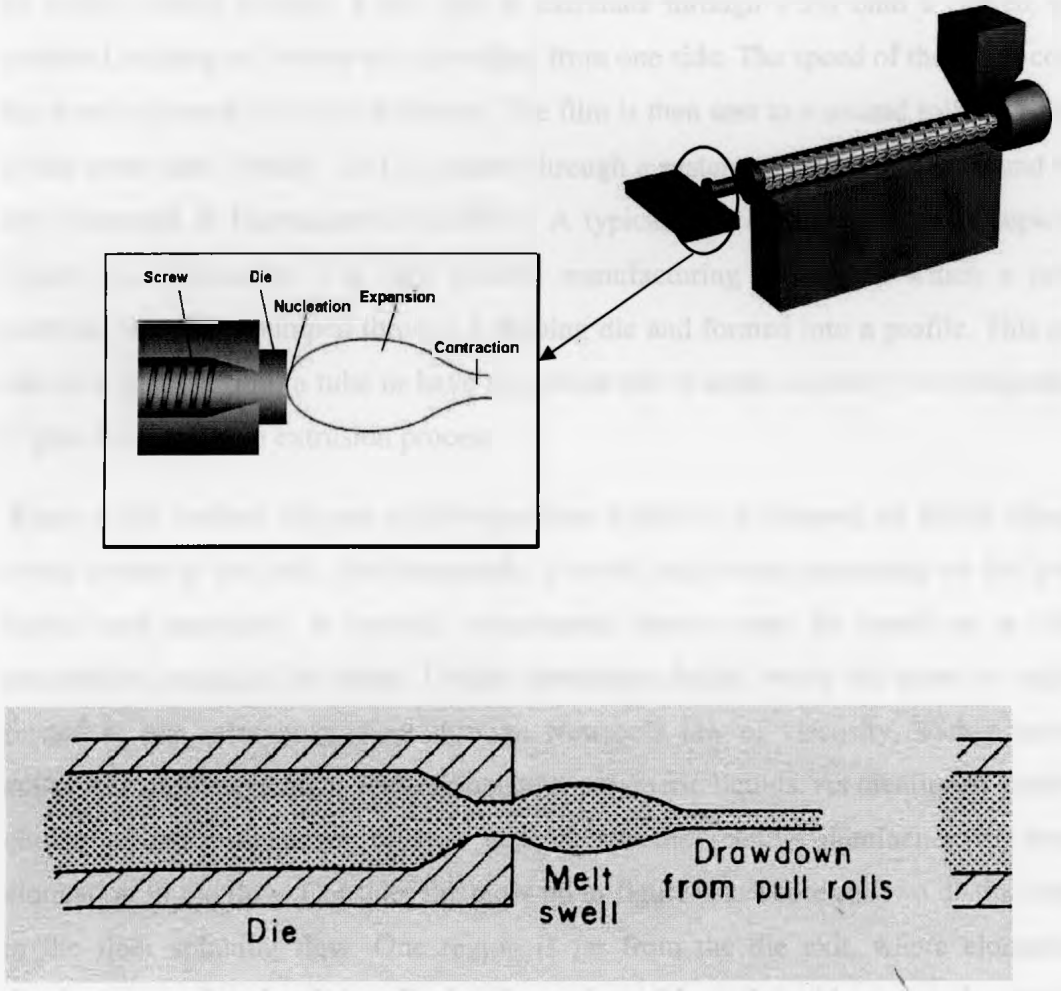

Figure 1.3 Schematic of extrusion process. A polymer material is melted, pumped through a shaping die and formed into a profile. This profile can be any shape for its cross section (Source: en.wikipedia.org)

In a film casting process, a thin film is extrudate through a slit onto a chilled, highly polished, turning roll where it is quenched from one side. The speed of the roller controls the draw ratio and final film thickness. The film is then sent to a second roller for cooling of the other side. Finally, the film passes through a system of rollers and is wound onto a roll (Osswald & Hernandez-Ortiz 2006). A typical film casting process is depicted in figure 1.2. "Extrusion is a high volume manufacturing process in which a polymer material is melted, pumped through a shaping die and formed into a profile. This profile can be a plate, a film, a tube or have any shape for its cross section." (en.wikipedia.org) Figure 1.3 depicts an extrusion process.

When a free surface viscous jet emerges from a tube or a channel, an abrupt change in stress occurs at the exit. Simultaneously, a swell may occur depending on the level of inertia and elasticity. A realistic viscoelastic theory must be based on a realistic constitutive equation for stress. Unlike Newtonian fluids, where the stress is explicitly related to the velocity gradient through Newton's law of viscosity, such a universal explicit or implicit relation does not exist for polymeric liquids. As mentioned earlier, the choice of the constitutive relation depends on the relative dominance of shear or elongation in the flow. Consider the blow up in figure 1.1. There are two distinct regions in the fiber spinning flow. One region is far from the die exit, where elongation is dominant over shearing due to the drawing action of the roll. In this region, the velocity is essentially uniform across the fiber, but changes in the streamwise direction. In this case, $\frac{\partial u}{\partial x} >> \frac{\partial u}{\partial z}$. The second region is close to the die exit, where shearing tends to dominate over elongation, and is reflected by the Poiseuille character of the flow as the fluid emerges from the die. However, at the exit itself, elongation is still significant due to the jump in the streamwise velocity from a zero value at the wall (stick) to a non-zero value at the free surface (slip). The present work focuses on the region close to the exit, where shearing is assumed to be dominant.

Experiment suggests that swelling is enhanced for polymeric fluids emerging from a tube or channel due to contraction before the exit and unrelaxed stresses after exit (figure 1.3). This is illustrated here in figure 1.4 by the experiment of Prof. McKinley at MIT.

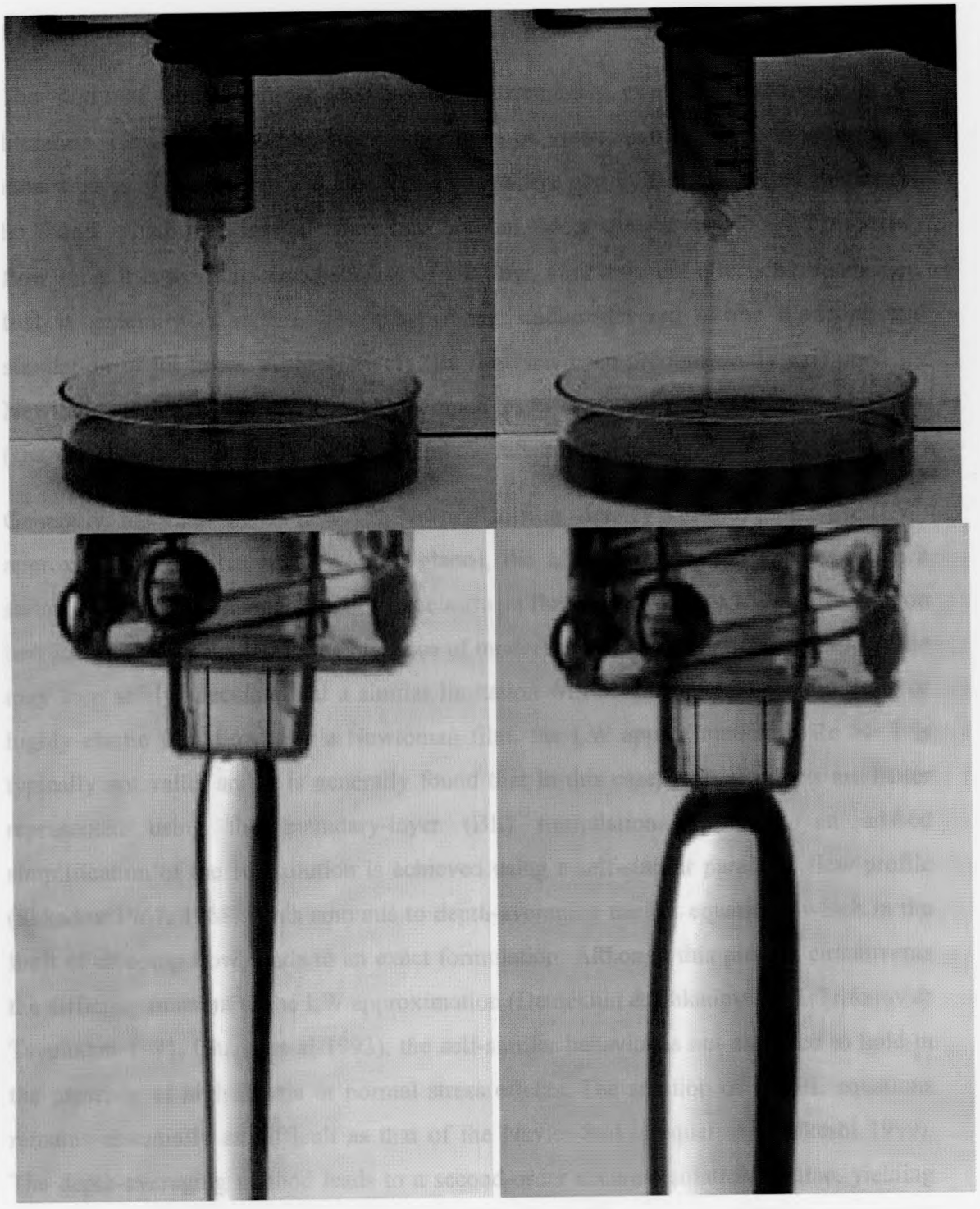

Figure 1.4 Experiment on die swell (source: http://web.mit.edu/nnf/.).

1.3 Literature review

The study of liquid laminar jets has been extensively examined previously in the literature. However, the focus has mainly been on Newtonian jet flow. In addition, in most studies of Newtonian jets, due to the convective non-linearities, limited studies can be found, which take inertial effect into account. Most studies also focused on steady flow since it is the long-term behavior of the flow, after transient effects have subsided, that is generally important. There are many studies devoted to the modeling and simulation of jet flows. Appreciatively, jet flow has been predominantly examined for Newtonian fluids (Chang 1994), and to a much lesser extent for non-Newtonian film flow (see, for instance Bérdaudo et al. 1998, and the references therein).

Generally, for small inertia flow of a Newtonian film, Benney's (1966) long wave (LW) approximation is often used. At first glance, the LW approximation appears to be a suitable choice for the modeling of viscoelastic jet flow. However, the LW approximation becomes seriously limited in the presence of moderate or high inertia (Chang 1994). One may then safely speculate that a similar limitation will be encountered for moderate or highly elastic film flow. For a Newtonian film, the LW approximation at $Re >> 1$ is typically not valid, and it is generally found that in this case, inertial effects are better represented using the boundary-layer (BL) formulation. Typically, an ad-hoc simplification of the BL solution is achieved using a self-similar parabolic flow profile (Shkadov 1967, 1968). This amounts to depth-averaging the BL equations, which in the limit of creeping flow, leads to an exact formulation. Although this process circumvents the difficulty inherent to the LW approximation (Demekhin & Shkadov 1985, Trifonov & Tsvelodub 1991, Chang et al 1993), the self-similar behavior is not expected to hold in the presence of high inertia or normal stress effects. The solution of the BL equations remains essentially as difficult as that of the Navier-Stokes equations (Takeshi 1999). The depth-averaging method leads to a second-order accurate solution in time, yielding plausible results, but raises a certain level of doubt in the presence of strong convective (and upper-convective) non-linearities due to the semi-parabolic assumption (Frenkel 1992; Takeshi 1999). The parabolic approximation is widely used in the literature and its

validity was established experimentally by Alekseenko, Narkoryakov, & Pokusaev (1985). However, it is generally argued that this validity holds only at low Reynolds number and provided that the surface waves are far from the entry (Wilkes 1962; Bertshy & Chin 1993). High inertia flow, turbulence, the presence of end effects, non-linear effects stemming from shear-thinning or viscoelastic effects are all factors that challenge the validity of the semi-parabolic profile.

A number of studies have been done to investigate the internal and free surface flows of viscoelastic fluids. However, most of the studies were focused on the flow inside the channel with low or negligible inertia. Gaidos and Darby (1988) reported the developing velocity and stress profiles in the entrance of a planar slit. Flow problems through a planar contraction were examined for the stress distribution (Kiriakidis et al. 1993), corner and lip vortex formation and flow behavior (Phillips and Williams 1999, Ganvir et al. 2007), and the role and importance of relaxation (Keshtiban et al. 2004) using different numerical schemes for both compressible and incompressible viscoelastic fluids. Among most recent studies, Rodd et al. (2010) showed the consequences of increasing the constriction length in microfluidic viscoelastic entry flows.

The free-surface flow of non-Newtonian fluids remains generally challenging. This is also true for thin film flow. Kang & Chen (1995) studied gravity-driven non-Newtonian films as well as creeping flow in the presence of surface tension effect. Bérdaudo et al (1998) examined the free-surface flow of a viscoelastic fluid emerging from various geometries. Khayat and coworkers have been examining extensively the highly non-linear flow, in the presence of inertia and/or elasticity, of thin films over rigid substrates of arbitrary shape. The planar flow of a Newtonian film was first considered over a stationary substrate (Khayat & Welke 2001; Khayat & Kim 2002) and a moving substrate (Tauqueer & Khayat 2004). The coating of shear-thinning (Kim and Khayat 2002) and viscoelastic (Khayat 2001) fluids were also considered on a planar substrate, and on axisymmetric substrates (Khayat & Kim 2006).

Generally, non-Newtonian jets are more likely to remain laminar compared to Newtonian jets (Rotem 1964; Cao et al. 2005; German & Khayat 2008). This makes the assumption

of laminar flow within a distance downstream more plausible. The axisymmetric free laminar jet of an incompressible pseudoplastic fluid was investigated by Rotem (1964). A BL approximation was used to find the velocity profiles for different exponents in an inelastic fluid. Submerged planar and axisymmetric jet flows of non-Newtonian power-law fluids at high Reynolds number have been investigated by Stehr & Schneider (2000). They used the method of matched asymptotic expansions and accounted for interaction between the jet flow and the induced flow.

Regarding the jet flow of viscoelastic fluids, the focus has mainly been in the literature on die swell and steady flow (see, for instance, Trang-Cong & Phan-Thien 1988, and, more recently, Liang et al. 1999). However, studies were done considering small or negligible inertia. Yuan et al. (1994) modeled the extrusion flow of viscoelastic fluid. Tome, Duffy & McKee (1996) examined the transient die swell and buckling of planar jets for Newtonian and generalized non-Newtonian fluids. Liang et al. (1999) carried out flow visualization and measurement of free surface to describe the behavior of a steady viscoelastic jet issuing from a capillary or an orifice under gravity. Their experiments revealed that depending upon the elasticity level of the fluid, the jet width may increase, decrease or remain unchanged downstream from the exit at least within a certain distance from the exit. In this case, the interplay between gravity and elasticity dictates the jet behavior. Mitsoulis (1999) studied the flow of an upper convected Maxwell model fluid through an abrupt expansion and more recently, the rheological behavior of dilute polymer solutions to understand the swell, excess pressure loss as well as the shape and the extent of the free surface under gravity (2010). His results showed the dependency of extrudate swell on elasticity levels, although the maximum swell was over predicted. Surface tension jet breakup of non-Newtonian fluids has also been examined both theoretically (Bousfield et al.1986) and experimentally (Christanti & Walker 2001). The transient response resulting from the spreading of surfactant on a thin weakly viscoelastic film has also been examined theoretically by Zhang, Matar & Craster (2002). Poole et al. (2007) reported velocity profiles using a systematic numerical investigation of model viscoelastic fluids through a planar sudden expansion. They observed a velocity overshoot upstream of the expansion with increasing Deborah number. Karapetsas and

Tsamopoulos (2008) studied the steady extrusion of viscoelastic materials from annular die following the PTT constitutive law. The mixed finite element method has been used to capture large deformations of the free surface as the liquid exits the die. Their study revealed the important role that the solvent viscosity can play in addition to the fluid elasticity and extensional viscosity. Tome et al. (2008) have developed a numerical method to analyze three dimensional unsteady viscoelastic free surface flows governed by Oldroyd-B constitutive equation and more recently, for the flows governed by Phan-Thien-Tanner constitutive equation (2010) using a finite difference technique. Their analysis provided the swell ratios for different Weissenberg number.

The upper convected Maxwell model or Oldroyd-B model has been used to study the behavior of viscoelastic fluids for many years. However, the results were only matching the experimental findings in the limit of low shear rates (Crochet and Keunings 1982, Chai and Yeow 1988, Bush 1990), whereas all important and exciting elastic flow phenomena were occurring at higher rates. Moreover, the behavior of the Oldroyd-B model in two important flows in the die swell problem, namely steady shear flow and steady elongational flow, were also found unrealistic (Tanner et al. 1985). Despite the limitations, this has been an attractive model to researchers as an initiative because of the relative simplicity. This model has a constant viscosity and single relaxation time that help to achieve convergence in the simulations.

Although studies were done for small or negligible inertia, there are applications, such as high speed film casting, where inertia plays significant role. Therefore, the objective of the present study is to examine the interplay among inertia, elasticity and gravity in the presence of surface tension for a polymer jet. The formulation and simulation are carried out for a two-dimensional jet flow in order to better understand the intricate flow structures for a viscoelastic jet. The problems associated with frequent mesh resizing needed for the rapid spatio-temporal variations in the flow field make conventional solutions schemes such as finite-element/difference methods unsuitable. For the pressure/gravity driven flow in this study, a weighted residual approach is adopted for a viscoelastic fluid with a generalized BL formulation proposed. The system is first

mapped onto a rectangular domain, followed by the expansion of the velocity field in terms of orthonormal basis functions. The Galerkin projection is used to derive the equations that govern the coefficients of expansion, which are then integrated numerically. This formulation is similar to the one adopted by Khayat & Kim (2006) for coating flow, and by German & Khayat (2005) for thin-jet flow of a Newtonian fluid. Unlike the depth-averaging method, the weighted residual methodology proposed becomes particularly suited for the early onset of wave propagation near the channel exit in the presence of strong normal-stress effect. The numerical results are compared and validated with the experimental results from Liang et al. (1999). The experiment was done using Boger fluid, which is a polymeric solution consisting of 94.86% polybutene (PB, Amoco H-300); 4.83% tetradecane solvent (C14); 0.31% polyisobutylene (PIB, Scientific Polymers, MW= 6 X 10^6). This polymeric fluid is a liquid at room temperature and exhibits thermal, mechanical and chemical stability. Since it is transparent it is suitable for optical measurements of free surface profile (shape and positions) of the jet (Liang et al. 1999).

CHAPTER 2

PROBLEM FORMULATION AND SOLUTION PROCEDURE

In this chapter, the governing equations are introduced, including the scaled conservation and constitutive equations, as well as the boundary and initial conditions for a viscoelastic thin fluid jet. Also included in this chapter is the solution procedure.

2.1 Problem formulation

The fluid examined in this study is assumed to be an incompressible polymeric solution represented by a single relaxation time and constant viscosity. The fluid properties include the density ρ, viscosity μ, and relaxation time λ. The solution viscosity $\mu = \mu_s + \mu_p$ comprises the Newtonian solvent viscosity μ_s and polymeric solute viscosity μ_p. Regardless of the nature of the fluid, the continuity and momentum conservation equations must hold. For an incompressible fluid, the conservation equations are:

$$\nabla \cdot \mathbf{U} = 0, \quad \rho\left(\mathbf{U}_T + \mathbf{U} \cdot \nabla \mathbf{U}\right) = \nabla \cdot \boldsymbol{\Sigma} + \rho \mathbf{g} \tag{2.1}$$

where $\mathbf{U}$ is the velocity vector, $\mathbf{g}$ is the gravitational acceleration, T is time, ∇ is the gradient operator, and $\boldsymbol{\Sigma}$ is the stress tensor. There are two components making up the deviatoric part of the stress tensor, a Newtonian constituent (solvent), and a polymeric constituent (solute) $\mathbf{T}$. The stress tensor is then expressed as

$$\Sigma = -\mathbf{P}\mathbf{I} + \mu_s\left(\nabla \mathbf{U} + \nabla \mathbf{U}^T\right) + \mathbf{T} \tag{2.2}$$

where the hydrostatic pressure is represented by P, and matrix transposition is denoted by superscript T. The polymeric constitutive equation for $\mathbf{T}$ is taken to correspond to an Oldroyd-B fluid and is written in the form (Bird, Armstrong & Hassager 1987):

$$\lambda\left(\mathbf{T}_T + \mathbf{U} \cdot \nabla \mathbf{T} - \mathbf{T} \cdot \nabla \mathbf{U} - \nabla \mathbf{U}^T \cdot \mathbf{T}\right) + \mathbf{T} = \mu_p\left(\nabla \mathbf{U} + \nabla \mathbf{U}^T\right) \tag{2.3}$$

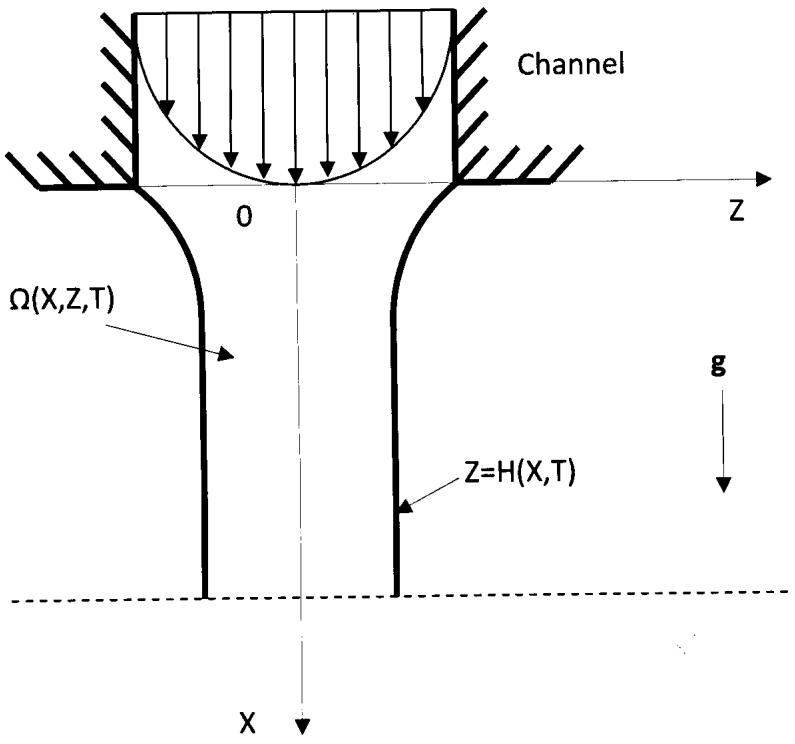

Figure 2.1 Schematic illustration of two-dimensional jet flow emerging from a vertical channel.

The equation for a Maxwell fluid is recovered in the limit $\mu_s \rightarrow 0$ in equations (2.1)-(2.3), and the limit $\mu_p \rightarrow 0$ leads to the Navier-Stokes equations. The problem is now examined using a Cartesian coordinate system using standard notations for velocity and stress components.

2.1.1 General equations and boundary conditions for 2D viscoelastic fluid

Consider again the general flow in figure 2.1. In this case, the equations (2.1) to (2.3) become

$$\frac{\partial U}{\partial X}+\frac{\partial W}{\partial Z}=0$$

$$\rho\left(\frac{\partial U}{\partial T}+U\frac{\partial U}{\partial X}+W\frac{\partial U}{\partial Z}\right)=-\frac{\partial P}{\partial X}+\mu_s\left(\frac{\partial^2 U}{\partial X^2}+\frac{\partial^2 U}{\partial Z^2}\right)+\frac{\partial T_{XX}}{\partial X}+\frac{\partial T_{XZ}}{\partial Z}+\rho g$$

$$\rho\left(\frac{\partial W}{\partial T}+U\frac{\partial W}{\partial X}+W\frac{\partial W}{\partial Z}\right)=-\frac{\partial P}{\partial Z}+\mu_s\left(\frac{\partial^2 W}{\partial X^2}+\frac{\partial^2 W}{\partial Z^2}\right)+\frac{\partial T_{ZX}}{\partial X}+\frac{\partial T_{ZZ}}{\partial Z}$$

From the constitutive equation for Oldroyd-B fluid,

xx-stress: $$\lambda\left(\frac{\partial T_{XX}}{\partial T}+U\frac{\partial T_{XX}}{\partial X}+W\frac{\partial T_{XX}}{\partial Z}-2T_{XX}\frac{\partial U}{\partial X}-2T_{XZ}\frac{\partial U}{\partial Z}\right)+T_{XX}=2\mu_p\frac{\partial U}{\partial X}$$

zz-stress: $$\lambda\left(\frac{\partial T_{ZZ}}{\partial T}+U\frac{\partial T_{ZZ}}{\partial X}+W\frac{\partial T_{ZZ}}{\partial Z}-2T_{ZZ}\frac{\partial W}{\partial Z}-2T_{XZ}\frac{\partial W}{\partial X}\right)+T_{ZZ}=2\mu_p\frac{\partial W}{\partial Z}$$

xz-stress: $$\lambda\left(\frac{\partial T_{XZ}}{\partial T}+U\frac{\partial T_{XZ}}{\partial X}+W\frac{\partial T_{XZ}}{\partial Z}-T_{XX}\frac{\partial W}{\partial X}-T_{XZ}\frac{\partial W}{\partial Z}-T_{XZ}\frac{\partial U}{\partial X}-T_{ZZ}\frac{\partial U}{\partial Z}\right)$$
$$+T_{XZ}=\mu_p\left(\frac{\partial U}{\partial Z}+\frac{\partial W}{\partial X}\right)$$

The force at the free surface is balanced by surface tension effect. So, in the presence of surface tension,

$$t_x = \sigma_{xx} n_x + \sigma_{xz} n_z = \sigma n_x \frac{\partial n_x}{\partial X}$$

$$\Rightarrow \left(-P + 2\mu_s \frac{\partial U}{\partial X} + T_{XX} \right) n_x + \left[\mu_s \left(\frac{\partial U}{\partial Z} + \frac{\partial W}{\partial X} \right) + T_{XZ} \right] n_z = \sigma n_x \frac{\partial n_x}{\partial X}$$

$$t_z = \sigma_{zx} n_x + \sigma_{zz} n_z = \sigma n_z \frac{\partial n_x}{\partial X}$$

$$\Rightarrow \left[\mu_s \left(\frac{\partial U}{\partial Z} + \frac{\partial W}{\partial X} \right) + T_{XZ} \right] n_x + \left(-P + 2\mu_s \frac{\partial W}{\partial Z} + T_{ZZ} \right) n_z = \sigma n_z \frac{\partial n_x}{\partial X}$$

These are the dynamic boundary conditions in x and z direction. The components of the normal vector are given by

$$n_x = \frac{H_X}{\sqrt{H_X{}^2 + 1}}$$

$$n_z = \frac{-1}{\sqrt{H_X{}^2 + 1}}$$

$$\text{and } \frac{\partial n_x}{\partial X} = \frac{H_{XX}}{\left(H_X{}^2 + 1 \right)^{3/2}}$$

The kinematic boundary condition describes the flow velocity in transverse direction, which is equal to the change of surface height with time.

$$W = \frac{dH}{dT} = \frac{\partial H}{\partial T} + U \frac{\partial H}{\partial X}$$

As to the boundary conditions at the channel exit, the flow is assumed to be of the Poiseuille type, which is now derived.

Consider a two dimensional incompressible plane viscous flow between parallel plates a distance D apart. The plates are assumed very wide and very long, so that the flow is essentially axial, $U \neq 0$ but $W = 0$. Considering only pressure varies along X direction,

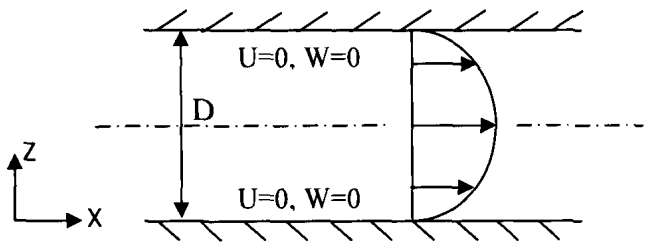

Figure 2.2: Definition diagram for Poiseuille flow.

conservation of mass equation is satisfied readily and leads to the conclusion that $U = U(Z)$. Considering steady state and neglecting gravity, the X and Z- momentum equations give

$$\frac{\partial P}{\partial X} = \mu_s \frac{\partial^2 U}{\partial Z^2} + \frac{\partial T_{XZ}}{\partial Z}$$

$$\frac{\partial P}{\partial Z} = \frac{\partial T_{ZZ}}{\partial Z}$$

Solving for the stresses,

$$T_{XX} = 2\lambda T_{XZ} \frac{\partial U}{\partial Z}$$

$$T_{ZZ} = 0$$

$$T_{XZ} = \mu_p \frac{\partial U}{\partial Z}$$

So, upon substituting the shear stress in the x-momentum equation, one obtains the same equation as for a Newtonian fluid

$$\frac{d^2 U}{dZ^2} = \frac{1}{\mu} \frac{dP}{dX}$$

The solution is accomplished by double integration,

$$U = \frac{1}{2\mu}\frac{dP}{dX}Z^2 + C_1 Z + C_2$$

The constants are found from the no-slip condition at each wall.

$$\text{for } U(Z=0) = 0, \qquad C_2 = 0$$

$$\text{for } U(Z=D) = 0, \qquad C_1 = -\frac{D}{2\mu}\frac{dP}{dX}$$

Thus, the flow in a channel due to pressure gradient is

$$U = \frac{1}{2\mu}\frac{dP}{dX}\left(Z^2 - DZ\right) \text{ and } \frac{dU}{dZ} = \frac{1}{2\mu}\frac{dP}{dX}(2Z - D)$$

The mean velocity inside the channel will be used as velocity scale. It is given by

$$U_0 = \frac{1}{D}\int_0^D U dZ = -\frac{D^2}{12\mu}\frac{dP}{dX}$$

In this case, the stress components become

$$T_{XZ} = \mu_p \frac{\partial U}{\partial Z} = \frac{\mu_p}{2\mu}\frac{dP}{dX}(2Z - D)$$

$$T_{XX} = 2\lambda T_{XZ}\frac{dU}{dZ} = 2\lambda\mu_p\left(\frac{dU}{dZ}\right)^2 = \frac{\lambda\mu_p}{2\mu^2}\left(\frac{dP}{dX}(2Z - D)\right)^2$$

The primary and secondary normal stresses become

$$N_1 = \Sigma_{xx} - \Sigma_{zz} = T_{xx} \text{ and } N_2 = \Sigma_{zz} - \Sigma_{yy} = 0.$$

2.1.2 Boundary-layer equations for a viscoelastic fluid

The flow of a viscoelastic jet emerging from a vertical channel is schematically depicted in figure 2.1 in the (X, Z) plane. The X-axis is chosen to correspond to the vertical (streamwise) direction and the Z-axis is chosen in the horizontal (transverse) direction. The domain of the fluid is represented by $\Omega(X, Z, T)$, with the (half) jet thickness denoted by $Z = H(X, T)$. The channel exit coincides with $X = 0$, and the (symmetric) flow is examined in the (X, Z) plane, with $Z = 0$ corresponding to the line of symmetry. The flow is induced by either a pressure gradient inside the channel and/or gravity, but for this study the emphasis will be on pressure-driven flow. The streamwise and transverse scale lengths are chosen to be a suitably defined length L, and the channel half width H_0, respectively. Since the film half thickness is of the same order as the boundary layer thickness, then $L \sim \frac{\rho U_0 H_0^2}{\mu}$. For both Newtonian and non-Newtonian fluids, there are four main dimensionless parameters. These are namely the Reynolds number, Re, the aspect ratio, ε, the Froude number, Fr and the Capillary number, Ca. Explicitly written, these take the following form:

$$\varepsilon \mathrm{Re} = \frac{\rho U_0 H_0^2}{\mu L} = O(1), \qquad \varepsilon = \frac{H_0}{L}, \qquad \mathrm{Fr}_L = \frac{U_0}{\sqrt{gL}}, \qquad \mathrm{Ca} = \frac{\mu U_o}{\sigma} \tag{2.4}$$

where the reference velocity, U_0, is the mean velocity in the channel in the absence of gravity. Note, in this case, that $\varepsilon \mathrm{Re} \sim O(1)$ and $\varepsilon \sim O\left(\mathrm{Re}^{-1}\right)$, where Re_H is the Reynolds based on H_0. Additional to these parameters are the similarity parameters for a viscoelastic flow, which include: the Deborah number, De, the solvent-to-solute viscosity ratio, Rv, and the solute-to-solution viscosity ratio, a:

$$\mathrm{De}_L = \frac{\lambda U_0}{L}, \qquad \mathrm{Rv} = \frac{\mu_s}{\mu_p}, \qquad a = \frac{\mu_p}{\mu} = \frac{1}{\mathrm{Rv}+1} \tag{2.5}$$

In this study, the fluid film is assumed thin with $\varepsilon << 1$. Thus, ε is taken as the perturbation parameter in order to reduce the formulation to that of the boundary-layer type. The scaling of the velocity, shear and normal stresses, and position coordinates take the following non-dimensional form:

$$x = \frac{X}{L}, \qquad z = \frac{Z}{H_0}, \qquad t = \frac{U_0 T}{L},$$
$$u = \frac{U}{U_0}, \qquad w = \frac{W}{\varepsilon U_0}, \qquad h = \frac{H}{H_0}, \qquad p = \frac{PL\varepsilon^2}{\mu U_0}, \tag{2.6a}$$

The non-linearities in the upper-convective terms create difficulty when scaling the stress equations. In general, one may set:

$$q = \frac{L\varepsilon^{\alpha}}{\mu U_0} T_{xx}, \quad s = \frac{L\varepsilon^{\beta}}{\mu U_0} T_{xz}, \quad r = \frac{L\varepsilon^{\gamma}}{\mu U_0} T_{zz} \tag{2.6b}$$

Note that the stress tensor is symmetric. The constants, α, β, γ are determined by ensuring that the terms in the conservation and constitutive equations balance. The reduced equations are derived in appendix A from the dimensionless form of equations (2.1) to (2.3), excluding terms of $O(\varepsilon^2)$ and higher.

In order for all the stress terms in the x-momentum equation to survive, the exponent α should be set equal to 2. Correspondingly, setting $\beta = 1$ ensures the survival of all the terms in the normal stress equation for q. It can be seen that this results in the streamwise normal stress q not depending strongly on the streamwise elongation term u_x, which should be the case for shear dominated (boundary-layer) flow. However, this stress does not disappear entirely due to the non-linear coupling with shear effects. With α and β set, the survival of the terms in the shear stress equation for s and normal stress equation for r can be achieved by setting $\gamma = 0$. The z-momentum equation now shows that the pressure gradient in the transverse direction is negligible, i.e. $p_z \sim 0(\varepsilon^2)$. This demonstrates that the pressure dependence in the transverse direction is negligible, which is in agreement with the limit of a Newtonian jet flow. Hence, assuming no body forces exist in the transverse

direction, the pressure is a function of the streamwise direction and time only. The conservation and constitutive equations are appended to take the following form:

$$u_x + w_z = 0 \tag{2.7a}$$

$$\varepsilon \mathrm{Re}\left(u_t + uu_x + wu_z\right) = -p_x + aRvu_{zz} + q_x + s_z + G_L \tag{2.7b}$$

$$p_z = 0 \tag{2.7c}$$

$$\mathrm{De}_L\left(q_t + uq_x + wq_z - 2su_z - 2qu_x\right) + q = 0 \tag{2.7d}$$

$$\mathrm{De}_L\left(r_t + ur_x + wr_z - 2sw_x - 2rw_z\right) + r = 2aw_z \tag{2.7e}$$

$$\mathrm{De}_L\left(s_t + us_x + ws_z - qw_x - ru_z\right) + s = au_z \tag{2.7f}$$

Here $G_L = \dfrac{\mathrm{Re}}{\mathrm{Fr}_L^2}$ is the gravity number. The equations above must be solved subject to the dynamic and kinematic conditions at the free surface, the symmetry conditions at z = 0, and the channel exit conditions at x = 0. The preceding scaling method was applied to the dynamic condition in the normal and tangential directions, resulting in

$$aRvu_z(x, z = h, t) + s(x, z = h, t) = q(x, z = h, t)h_x(x, t) \tag{2.8a}$$

$$p(x, z = h, t) = -\frac{\varepsilon^3}{\mathrm{Ca}} h_{xx} \tag{2.8b}$$

In dimensionless form, the kinematic condition becomes

$$w(x, z = h, t) = h_t(x, t) + u(x, z = h, t)h_x(x, t) \tag{2.9}$$

The flow conditions at the channel exit correspond to the flow inside an infinite channel. Thus

$$\left.\begin{aligned} u(x=0,z,t) &= \frac{1}{2}(3+G_L)\left(1-z^2\right) \\ w(x=0,z,t) &= 0 \\ q(x=0,z,t) &= 2aDe_L(3+G_L)^2 z^2 \\ r(x=0,z,t) &= 0 \\ s(x=0,z,t) &= -a(3+G_L)z \end{aligned}\right\} \tag{2.10a}$$

The jet thickness at the channel exit is assumed fixed, so that

$$h(x=0,z,t)=1 \tag{2.10b}$$

Finally, the symmetry conditions are

$$w(x,z=0,t)=u_z(x,z=0,t)=s(x,z=0,t)=0 \tag{2.11}$$

In this formulation it is assumed that no external force or pressure acts on the fluid surface. For a surface-pressure-driven flow the reader is referred to Kriegsmann, Miksis & Vanden-Broeck (1998). Also, since the pressure p does not depend on z, the pressure must vanish everywhere in order to satisfy the zero-pressure condition (2.8b). For this reason, the axial pressure gradient term of (2.7b) will no longer be included.

2.1.3 Rescaled problem

Now that the boundary-layer equations are derived, a more convenient scaling is introduced in terms of one velocity and one length scale. Thus, let

$$\begin{aligned} x' &= \frac{X}{H_0}, \qquad z = \frac{Z}{H_0}, \qquad t' = \frac{U_0 T}{H_0}, \\ u &= \frac{U}{U_0}, \qquad w' = \frac{W}{U_0}, \qquad h = \frac{H}{H_0}, \qquad p' = \frac{PH_0}{\mu U_0}, \end{aligned} \tag{2.12a}$$

$$q' = \frac{H_0}{\mu U_0}T_{xx}, \quad s' = \frac{H_0}{\mu U_0}T_{xz}, \quad r' = \frac{H_0}{\mu U_0}T_{zz} \tag{2.12b}$$

The non-dimensional parameters for the problem are now all given in terms of channel half width to read:

$$\mathrm{Re}=\frac{\rho U_0 H_0}{\mu},\qquad \mathrm{Fr}=\frac{U_0}{\sqrt{gH_0}},\qquad \mathrm{Ca}=\frac{\mu U_o}{\sigma},\qquad \mathrm{De}=\frac{\lambda U_0}{H_0},\qquad \mathrm{Rv}=\frac{\mu_s}{\mu_p} \tag{2.13}$$

The rescaled conservation and constitutive equations (2.7) take the following form (after dropping the prime):

$$u_x + w_z = 0 \tag{2.14a}$$

$$\mathrm{Re}\left(u_t + uu_x + wu_z\right) = aRvu_{zz} + q_x + s_z + \mathrm{Ca}^{-1}h_{xxx} + G \tag{2.14b}$$

$$\mathrm{De}\left(q_t + uq_x + wq_z - 2su_z - 2qu_x\right) + q = 0 \tag{2.14c}$$

$$\mathrm{De}\left(r_t + ur_x + wr_z - 2sw_x - 2rw_z\right) + r = 2aw_z \tag{2.14d}$$

$$\mathrm{De}\left(s_t + us_x + ws_z - qw_x - ru_z\right) + s = au_z \tag{2.14e}$$

Note that the pressure gradient is now eliminated after using condition (2.8b).

2.2 Solution procedure

Traditionally, for Newtonian thin-film flow, the equations are solved by imposing a semi-parabolic profile for the velocity and depth-averaging the equations across the thickness. The strong non-linear effects originating from inertia and normal stress for a viscoelastic fluid make this approach unfeasible. The solution process is obviously difficult due to the explicit z dependence of the velocity and stress components. Formal handling of the transverse flow expansion was suggested by (Zienkievicz & Heinrich 1979, Ruyer-Quil & Manneville 1998, Takeshi 1999). The present study follows closely and generalizes the work of Zienkievicz & Heinrich (1979), with the exception that the transverse velocity component will not be neglected and the change in surface height over time is also included.

2.2.1 Mapped equations

For the solution procedure, the equations are first mapped onto a rectangular domain in order to apply the weighted residual method. All flow variables are then expanded in terms of polynomial shape functions in the transverse direction. The Galerkin projection is then applied in order to generate the equations that determine the expansion coefficients. A Lagrangian time-stepping implicit finite-difference method is coupled with a fourth-order Runge-Kutta integration solution approach in the flow direction in order to determine the expansion coefficients. This is a similar approach as to the ones developed previously for two-dimensional coating flow of Newtonian (Khayat & Welke 2001), and generalized Newtonian fluids (Khayat and Kim 2002). The present formulation is quite involved and will only be summarized in this work. System (2.7) is reduced to a transient one-dimensional problem formulation by an expansion of the velocity and stress components in terms of orthonormal modes in the transverse direction. The following mapping is used:

$$\chi(x,z,t) = x, \quad \xi(x,z,t) = \frac{z}{h(x,t)}, \quad \tau(x,z,t) = t \tag{2.15}$$

with $\xi \in [0, 1]$.

Let v be a general function variable. Thus, one introduces the convective derivative as

$$\frac{dv}{d\tau} = v_\tau - \frac{\xi}{h}\left(h_\tau v_\xi + u v_\xi h_\chi\right) + u v_\chi + \frac{1}{h} w v_\xi \tag{2.16}$$

The mapped equations are as follows

$$u_\chi - \frac{\xi}{h} h_\chi u_\xi + w_\xi \frac{1}{h} = 0 \tag{2.17a}$$

$$Re\frac{du}{d\tau} = \frac{1}{h}\left(\frac{aRv}{h} u_{\xi\xi} - \xi h_\chi q_\xi + s_\xi\right) + q_\chi + Ca^{-1} h_{\chi\chi\chi} + G \tag{2.17b}$$

$$De\left[\frac{dq}{d\tau}-\frac{2}{h}su_\xi-2q\left(u_\chi-\frac{\xi}{h}h_\chi u_\xi\right)\right]+q=0 \tag{2.17c}$$

$$De\left[\frac{dr}{d\tau}+\frac{2}{h}\left(\xi sh_\chi w_\xi-rw_\xi\right)-2sw_\chi\right]+r=\frac{2a}{h}w_\xi \tag{2.17d}$$

$$De\left[\frac{ds}{d\tau}+\frac{1}{h}\left(\xi qh_\chi w_\xi-ru_\xi\right)-qw_\chi\right]+s=\frac{1}{h}au_\xi \tag{2.17e}$$

In the Newtonian limit, equations (2.17) reduce to

$$u_\chi-\frac{\xi}{h}h_\chi u_\xi+w_\xi\frac{1}{h}=0 \tag{2.18a}$$

$$Re\frac{du}{d\tau}=\frac{1}{h^2}u_{\xi\xi}+Ca^{-1}h_{\chi\chi\chi}+G \tag{2.18b}$$

2.2.2 Spectral expansion

The orthonormal shape functions $A_i(\xi)$, $B_i(\xi)$, $C_i(\xi)$ and $D_i(\xi)$ for the streamwise velocity, u, normal stress component q, and shear component stress s as well as the normal stress component r are shown as follows:

$$\left.\begin{aligned} u(\chi,\xi,\tau)&=\sum_{i=1}^{M}U_i(\chi,\tau)A_i(\xi), & q(\chi,\xi,\tau)&=\sum_{i=1}^{M}Q_i(\chi,\tau)B_i(\xi),\\ r(\chi,\xi,\tau)&=\sum_{i=1}^{M}R_i(\chi,\tau)C_i(\xi), & s(\chi,\xi,\tau)&=\sum_{i=1}^{M}S_i(\chi,\tau)D_i(\xi), \end{aligned}\right\} \tag{2.19}$$

where M represents the number of modes and the unknown coefficients are $U_i(\chi,\tau)$, $Q_i(\chi,\tau)$, $R_i(\chi,\tau)$ and $S_i(\chi,\tau)$. Also, generally, let $v(\chi,\xi,\tau)=\sum_{i=1}^{M}V_i(\chi,\tau)\psi_i(\xi)$. Equation (2.17a) becomes

$$U_{i\chi}A_i - \frac{1}{h}\left(\xi h_\chi U_i A_i' + w_\xi\right) = 0 \tag{2.20}$$

The transverse velocity component, w, is determined by integrating the continuity equation (2.20) to give

$$w(\chi,\xi,\tau) = h_\chi\left(\xi A_i - \phi_i\right)U_i - h\phi_i U_{i\chi} \tag{2.21}$$

where $\phi_i(\xi) = \int_0^\xi A_i d\xi$.

In this case, the convective terms are of the following form

$$\begin{aligned}\frac{dv}{d\tau} = {} & V_{j\tau}\psi_j - \frac{1}{h}V_j\psi_j'\left[\xi\left(h_\tau + h_\chi U_k A_k\right) - h_\chi\left(\xi A_k - \phi_k\right)U_k\right] \\ & + U_j A_j V_{k\chi}\psi_k - V_j\psi_j' U_{k\chi}\phi_k\end{aligned} \tag{2.22}$$

Equations (2.17b) to (2.17e) becomes

$$\mathrm{Re}\frac{du}{d\tau} = \frac{1}{h}\left[\frac{aRv}{h}U_j A_j'' - \xi h_\chi Q_j B_j' + S_j D_j'\right] + Q_{k\chi}B_k + \mathrm{Ca}^{-1}h_{\chi\chi\chi} + G \tag{2.23a}$$

$$\mathrm{De}\left[\frac{dq}{d\tau} + \frac{2}{h}U_j A_j'\left(\xi h_\chi Q_k B_k - S_k D_k\right) - 2Q_j B_j U_{k\chi}A_k\right] + Q_j B_j = 0 \tag{2.23b}$$

$$\begin{aligned}\mathrm{De}\Bigg[\frac{dr}{d\tau} + 2\sum_{j=1}^{M} S_j D_j\Bigg[& h_\chi\left\{\frac{\xi h_\chi}{h}U_k\left(\xi A_k' + A_k - \phi_k'\right) - U_{k\chi}\phi_k'\right\} \\ & - \left\{\left(\xi A_k - \phi_k\right)\left(h_\chi U_k\right)_\chi - \phi_k\left(hU_{k\chi}\right)_\chi\right\}\Bigg] - 2R_j C_j\left\{\frac{h_\chi}{h}\left(\xi A_k' + A_k - \phi_k'\right)U_k\right. \\ & \left. - U_{k\chi}\phi_k'\right\}\Bigg] + R_j C_j = \frac{2a}{h}\left[h_\chi\left(\xi A_j' + A_j - \phi_j'\right)U_j - hU_{j\chi}\phi_j'\right]\end{aligned} \tag{2.23c}$$

$$De\left[\frac{ds}{d\tau}+Q_jB_j\left[h_\chi\left\{\frac{\xi h_\chi}{h}U_k\left(\xi A_k{}'+A_k-\phi_k{}'\right)-\xi U_{k\chi}\phi_k{}'\right\}-\left\{\left(\xi A_k-\phi_k\right)\left(h_\chi U_k\right)_\chi\right.\right.\right.$$
$$\left.\left.\left.-\phi_k\left(hU_{k\chi}\right)_\chi\right\}\right]-\frac{1}{h}U_jA_j{}'R_kC_k\right]+S_jD_j=\frac{a}{h}U_jA_j{}' \qquad (2.23d)$$

where a prime denotes a total differentiation. In addition to the condition of orthonormality, the shape functions must also satisfy various boundary conditions. Some of these conditions are not obvious. One condition is the limit of Newtonian film flow being recovered for this viscoelastic formulation as $Rv \to \infty$. One major difficulty for viscoelastic flow, as opposed to a Newtonian flow, is that the shear stress does not simply and necessarily vanish at the free surface. This becomes apparent when examining condition (2.8a), and also noting that there does not exist separate boundary conditions on shear and normal stresses. This, however, can be remedied by satisfying condition (2.8a) as well as recovering the Newtonian limit by simply setting the shear and normal stresses equal to zero at the free surface. Hence, assuming orthonormality, the following conditions apply for A_i:

$$\left\langle A_iA_j\right\rangle=\delta_{ij}, \qquad A_i'(\xi=0)=A_i'(\xi=1)=0 \qquad (2.24a)$$

which satisfy conditions (2.11). Here, δ_{ij} is the Kronecker delta, and $\langle\ \rangle$ denotes the integration over the interval $\xi \in [0, 1]$. Note that a prime denotes total differentiation. For B_i, it is not difficult to deduce from equation (2.7d) that, given the symmetry conditions (2.11), q is also symmetric with respect to the centreline. Thus

$$\left\langle B_iB_j\right\rangle=\delta_{ij}, \qquad B_i{}'(\xi=0)=0 \qquad (2.24b)$$

Note that q(x, z = 0) does not necessarily vanish, unless q(x = 0, z = 0) = 0. The boundary conditions for C_i are not as obvious. Nothing for certain can be said about r at either the free surface or line of symmetry. In this case, the corresponding shape function is assumed to satisfy only the condition of orthonormality, namely

$$\langle C_i C_j \rangle = \delta_{ij} \tag{2.24c}$$

Upon use of equations (2.18a) and (2.21), the kinematic condition (2.9) becomes

$$h_\chi = -\frac{h}{\overline{U}} U_{i\chi} \langle A_i \rangle - \frac{h_\tau}{\overline{U}} \tag{2.25}$$

where, $\overline{U} = U_i \langle A_i \rangle$

While carrying out the Galerkin Projection, the general form of the convective terms become, from expression (2.22)

$$\begin{aligned} \left\langle \frac{dv}{d\tau} \psi_i \right\rangle = V_{i\tau} - \frac{1}{h} V_j \left[h_\tau \left\langle \xi \psi_j' \psi_i \right\rangle + h_\chi U_k \left\langle \phi_k \psi_j' \psi_i \right\rangle \right] \\ + U_j V_{k\chi} \left\langle A_j \psi_k \psi_i \right\rangle - V_j U_{k\chi} \left\langle \phi_k \psi_j' \psi_i \right\rangle \end{aligned} \tag{2.26}$$

Equations (2.23a) to (2.23d) become

$$\begin{aligned} \mathrm{Re} \left\langle \frac{du}{d\tau} A_i \right\rangle = \frac{1}{h} \left(\frac{aRv}{h} U_j \left\langle A_j'' A_i \right\rangle + S_j \left\langle D_j' A_i \right\rangle - h_\chi Q_j \left\langle \xi B_j' A_i \right\rangle \right) \\ + Q_{j\chi} \left\langle A_i B_j \right\rangle + Ca^{-1} h_{\chi\chi\chi} \langle A_i \rangle + G \langle A_i \rangle \end{aligned} \tag{2.27a}$$

$$\begin{aligned} \mathrm{De} \left[\left\langle \frac{dq}{d\tau} B_i \right\rangle + \frac{2}{h} U_j \left(h_\chi Q_k \left\langle \xi A_j' B_k B_i \right\rangle - S_k \left\langle A_j' D_k B_i \right\rangle \right) \right. \\ \left. - 2 Q_j U_{k\chi} \left\langle B_j A_k B_i \right\rangle \right] + Q_i = 0 \end{aligned} \tag{2.27b}$$

$$\begin{aligned} \mathrm{De} \left[\left\langle \frac{dr}{d\tau} C_i \right\rangle + 2 S_j \left[h_\chi \left\{ \frac{h_\chi}{h} U_k \left\langle \xi \left(\xi A_k' + A_k - \phi_k' \right) D_j C_i \right\rangle - U_{k\chi} \left\langle \xi \phi_k' D_j C_i \right\rangle \right\} \right. \right. \\ \left. - \left\{ \left(h_\chi U_k \right)_\chi \left\langle \left(\xi A_k - \phi_k \right) D_j C_i \right\rangle - \left(h U_{k\chi} \right)_\chi \left\langle \phi_k D_j C_i \right\rangle \right\} \right] \\ \left. - 2 R_j \left\{ \frac{h_\chi}{h} \left\langle \left(\xi A_k' + A_k - \phi_k' \right) C_j C_i \right\rangle U_k - U_{k\chi} \left\langle \phi_k' C_j C_i \right\rangle \right\} \right] \\ + R_i = \frac{2a}{h} \left[h_\chi \left\langle \left(\xi A_j' + A_j - \phi_j' \right) C_i \right\rangle U_j - h U_{j\chi} \left\langle \phi_j' C_i \right\rangle \right] \end{aligned} \tag{2.27c}$$

$$De\left[\left\langle\frac{ds}{d\tau}D_i\right\rangle+Q_j\left[h_\chi\left\{\frac{h_\chi}{h}U_k\left\langle\xi\left(\xi A_k{}'+A_k-\phi_k{}'\right)B_jD_i\right\rangle-U_{k\chi}\left\langle\xi\phi_k{}'B_jD_i\right\rangle\right\}\right.\right.$$
$$\left.\left.-\left\{\left(h_\chi U_k\right)_\chi\left\langle\left(\xi A_k-\phi_k\right)B_jD_i\right\rangle-\left(hU_{k\chi}\right)_\chi\left\langle\phi_kB_jD_i\right\rangle\right\}\right]\right. \tag{2.27d}$$
$$\left.-\frac{1}{h}U_jR_k\left\langle A_j{}'C_kD_i\right\rangle\right]+S_i=\frac{a}{h}U_j\left\langle A_j{}'D_i\right\rangle$$

The insertion of expression (2.21) into the governing equations allows the elimination of w. Using expression (2.21), condition (2.9) becomes

$$h_\tau+hU_{j\chi}\left\langle A_j\right\rangle+h_\chi U_j\left\langle A_j\right\rangle=h_\tau+E8_i\left(hU_{i\chi}+h_\chi U_i\right)=0 \tag{2.28}$$

In compact form, expression (2.26) becomes

$$\left\langle\frac{dv}{d\tau}\psi_i\right\rangle=V_{i\tau}-\frac{1}{h}V_j\left[h_\tau\alpha1_{ij}+h_\chi U_k\alpha2_{ijk}\right]+U_jV_{k\chi}\alpha3_{ijk}-V_jU_{k\chi}\alpha2_{ijk} \tag{2.29}$$

where $\alpha1_{ij}=\left\langle\xi\psi_j{}'\psi_i\right\rangle$, $\alpha2_{ijk}=\left\langle\phi_k\psi_j{}'\psi_i\right\rangle$ and $\alpha3_{ijk}=\left\langle A_j\psi_k\psi_i\right\rangle$.

Now, equations (2.27a) to (2.27d) become

$$Re\left\langle\frac{du}{d\tau}A_i\right\rangle=\frac{1}{h}\left(\frac{aRv}{h}U_jE4_{ij}+S_jE5_{ij}-h_\chi Q_jE6_{ij}\right)+Q_{j\chi}E7_{ij}$$
$$+Ca^{-1}h_{\chi\chi\chi}E8_i+GE8_i \tag{2.30a}$$

$$De\left[\left\langle\frac{dq}{d\tau}B_i\right\rangle+\frac{2}{h}U_j\left(h_\chi Q_kF4_{ijk}-S_kF5_{ijk}\right)-2Q_jU_{k\chi}F6_{ijk}\right]+Q_i=0 \tag{2.30b}$$

$$De\left[\left\langle\frac{dr}{d\tau}C_i\right\rangle+2S_j\left[h_\chi\left\{\frac{h_\chi}{h}U_kG4_{ijk}-U_{k\chi}G5_{ijk}\right\}-\left\{\left(h_\chi U_k\right)_\chi G6_{ijk}-\left(hU_{k\chi}\right)_\chi G7_{ijk}\right\}\right]\right.$$
$$\left.-2R_j\left\{\frac{h_\chi}{h}U_kG8_{ijk}-U_{k\chi}G9_{ijk}\right\}\right]+R_i=\frac{2a}{h}\left[h_\chi U_jG10_{ij}-hU_{j\chi}G11_{ij}\right] \tag{2.30c}$$

$$De\left[\left\langle\frac{ds}{d\tau}D_i\right\rangle+Q_j\left\{h_\chi\left(\frac{h_\chi}{h}U_kH4_{ijk}-U_{k\chi}H5_{ijk}\right)-\left(\left(h_\chi U_k\right)_\chi H6_{ijk}-\left(hU_{k\chi}\right)_\chi H7_{ijk}\right)\right\}\right.$$
$$\left.-\frac{1}{h}U_jR_kH8_{ijk}\right]+S_i=\frac{a}{h}U_jH9_{ij} \tag{2.30d}$$

The corresponding boundary conditions are derived from (2.10a) become

$$\left.\begin{aligned}
&U_i(\chi=0,\tau)=\frac{(3+G)}{2}\left\langle\left(1-\xi^2\right)A_i(\xi)\right\rangle=\frac{(3+G)}{2}E0_i\\
&Q_i(\chi=0,\tau)=2aDe(3+G)^2\left\langle\xi^2B_i(\xi)\right\rangle=2aDe(3+G)^2F0_i\\
&R_i(\chi=0,\tau)=0,\\
&S_i(\chi=0,\tau)=-a(3+G)\langle\xi D_i(\xi)\rangle=-a(3+G)H0_i\\
&h(\chi=0,\tau)=1
\end{aligned}\right\} \tag{2.31}$$

The expressions for different E, F, G and H are given in appendix B.

In the Newtonian limit, equations (2.30) reduce to

$$Re\left\langle\frac{du}{d\tau}A_i\right\rangle=\frac{aRv}{h^2}U_jE4_{ij}+Ca^{-1}h_{\chi\chi\chi}E8_i+GE8_i \tag{2.32}$$

This is analogous to Newtonian and generalized Newtonian flows (Khayat & Welke 2001; Kim & Khayat 2002). The expansion coefficients are obtained upon substitution of expansions (2.19) along with (2.21) into equations (2.14). These equations are then multiplied by the appropriate shape function and integrated over the interval $\xi \in [0, 1]$. This results in a system of 4M + 1 partial differential equations in the (χ, τ) domain. These equations are then solved using a Lagrangian implicit finite-difference discretization scheme accompanied by a 4^{th} order Runge-Kutta integration method in the x- or χ-direction.

CHAPTER 3

RESULTS AND DISCUSSION

The formulation and numerical implementation above are now used to study the flow of a thin jet emerging from the channel as illustrated schematically in figure 2.1. The physical domain of the fluid is assumed to extend from $x = 0$ to $x \to \infty$, but the computational domain will be restricted to $x \in [0, 10]$. The influence of fluid inertia, gravity and surface tension is investigated at moderately high Reynolds number in order not to make inertia dominant.

3.1 Newtonian jet flow

The investigation of the steady Newtonian jet begins with analysis of the rate of convergence of modes. The number of modes required for reasonable convergence is typically small because of the predominantly slow variation of the flow field in the transverse direction. Figure 3.1 illustrates the rate of convergence in the absence of gravity and surface tension for a flow at $Re = 20$. The figure shows the surface height, $h(x)$, plotted against position, x, for different number of modes. Convergence is essentially achieved by including only a few modes ($M < 6$), especially far downstream from the channel exit. A similar rate of convergence is observed for other flow variables and will not be reported here.

Influence of inertia on Newtonian jet flow is first examined by varying the Reynolds number. Figure 3.2 illustrates the influence of inertia for $Re \in [20, 100]$. The flow is illustrated in the figure, where the height of the free surface $h(x)$, streamwise velocity $u(x, z = h)$ and transverse velocity at the free surface $w(x, z = h)$ are plotted against x for a given Reynolds number. Since mass is conserved, the (average) steady streamwise velocity behaves like the inverse of the film height (see figure 3.2b).

The film profiles in figure 3.2a show a monotonic response of the jet thickness with respect to position, with a strong contraction in film height close to the channel exit. This

contraction is weakened by inertia. The curves in the figure suggest, as expected, that in the limit of infinite Reynolds number, the jet thickness remains constant with x. In fact, the contraction ratio for a Newtonian jet is always same. However, the distance required for the jet to reach uniform condition does depend and indeed increases with inertia. The distance becomes infinite in infinite Reynolds number. The contraction in height is accompanied by a sharp drop in transverse velocity (see figure 3.2c), which reaches a minimum at a location close to the channel exit that is essentially independent of inertia. Note that plug flow conditions are reached far downstream from the channel exit at any Reynolds number, which is also reflected by the constancy of streamwise velocity component in figure 3.2b.

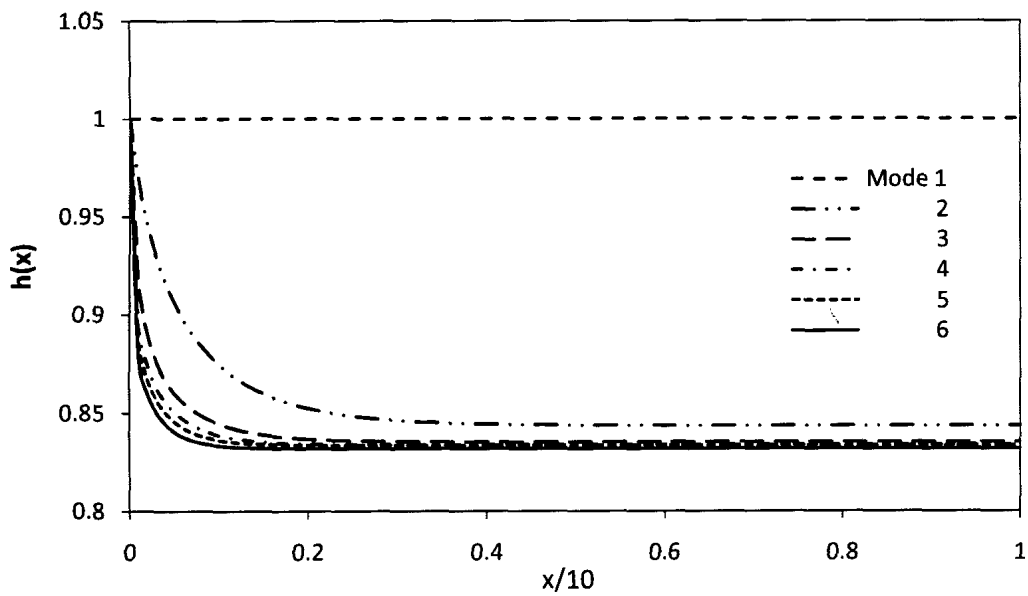

Figure 3.1 Convergence rate and influence of the number of modes in the absence of gravity and surface tension (G = We = 0) and Re = 20.

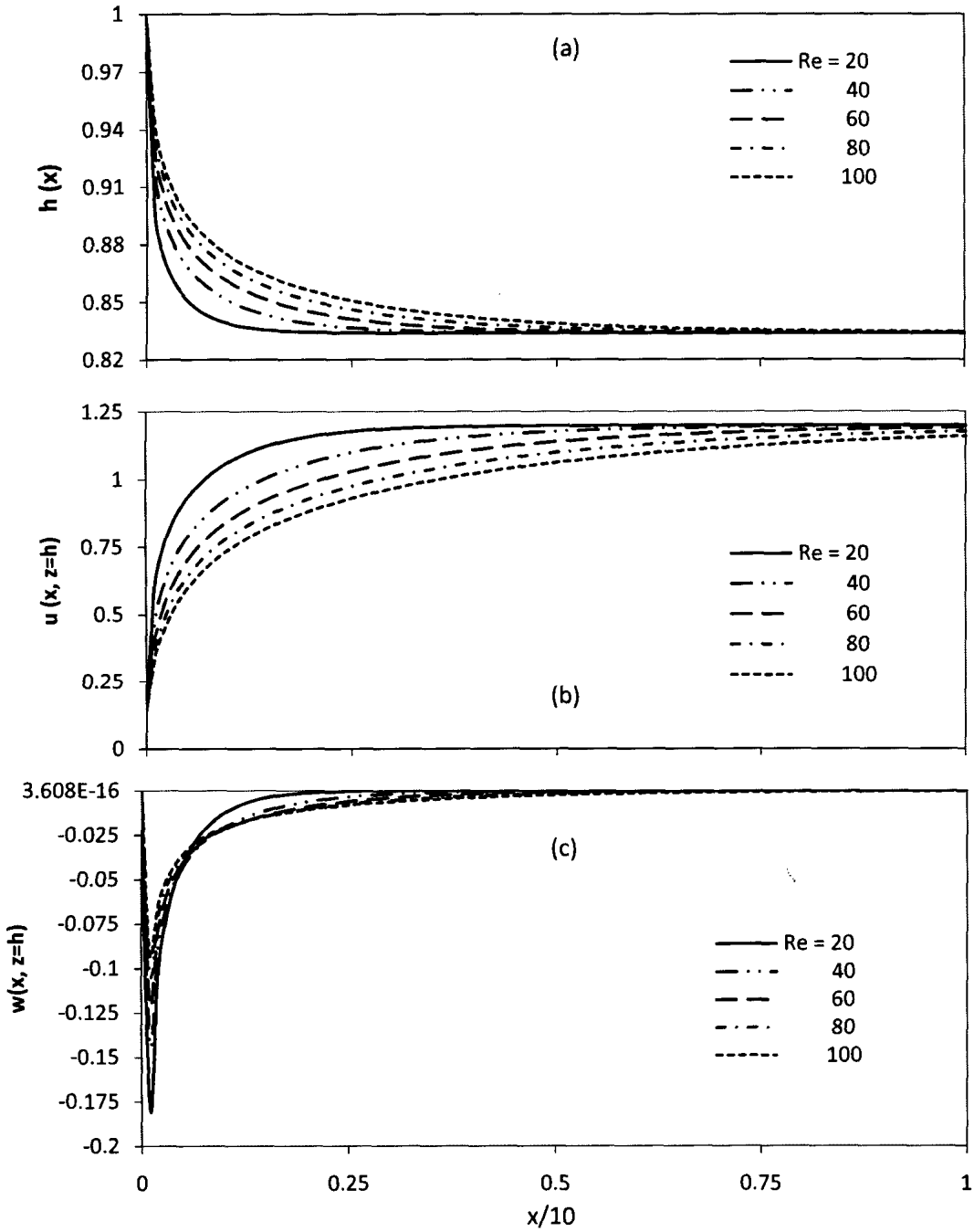

Figure 3.2 Influence of inertia on (a) jet thickness, (b) streamwise velocity and (c) surface transverse velocity in the absence of gravity and surface tension (G = We = 0), for Re $\in$ [20, 100].

Further insight on the role of inertia is inferred from figure 3.3. The jet thickness, streamwise velocity and transverse velocity are plotted as a function of Re, respectively, at the location, x_m, of minimum w. The flow response is obviously monotonic with respect to Re. Figures 3.3a, 3.3b and 3.3c show that the flow is strongly dependent on inertia for small Reynolds number. In fact, as $Re \rightarrow 0$, the jet tends to infinitely contract near $x = 0$ and reach the uniform thickness immediately. In this limit, $w \rightarrow -\infty$ (not shown). This behavior is exactly opposite to that encountered in the flow exiting a channel and flowing over a rigid plate (as in coating flow). In this case, the film thickness tends to grow infinitely in the limit $Re \rightarrow 0$, indicating that the film tends to accumulate near the channel exit, resisting flow (see Khayat and Welke 2001). This contrast in flow behavior has a dramatic fundamental and practical consequence if one views the flow of the jet film as equivalent to the flow of a thin film over a fully lubricated (rigid) plate. This becomes particularly relevant in the case of polymeric film flow over a flat plate where slippage can occur. The difference between the two situations originates from the difference in boundary conditions, namely stick as opposed to slip at $z = 0$.

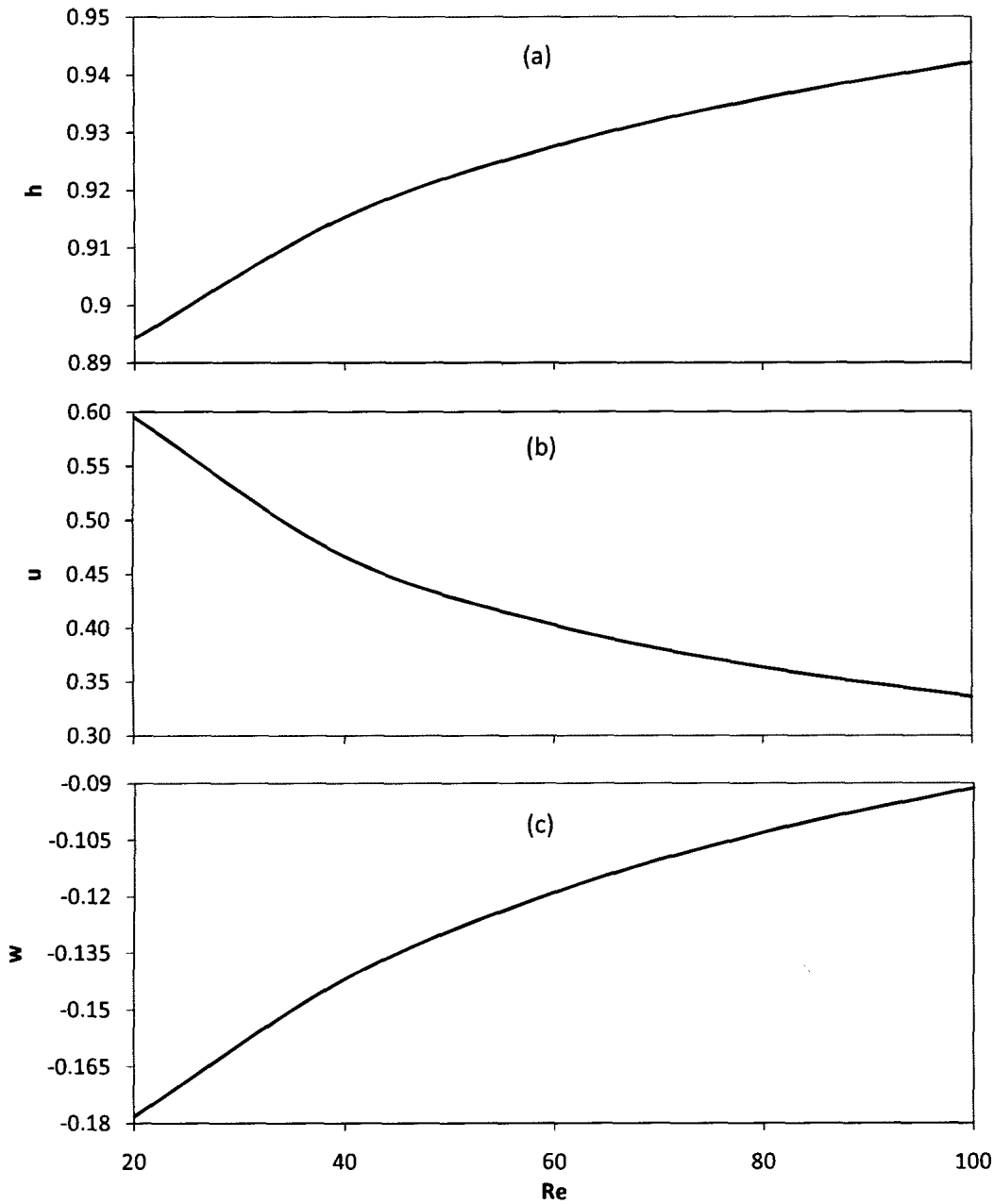

Figure 3.3 Influence of inertia on the (a) Jet thickness, (b) streamwise velocity and (c) transverse velocity the location, $x = x_m$, of minimum w.

Figure 3.4 illustrates the influence of inertia for Re $\in$ [20, 100] in the presence of surface tension but in the absence of gravity. These figures show an opposite trend compared to the effect of inertia in the absence of surface tension and gravity (see figure 3.2). However, the flow does not always respond in this manner to the influence of surface tension. This is somewhat reflected in figure 3.4c, where the location of the minimum in w does not depend monotonically on We. Other trends are possible depending on the level of surface tension. Indeed, for small We value, the flow responds similarly to the absence of surface tension.

The influence of gravity is illustrated in figure 3.5 in the absence of surface tension for the range G $\in$ [0, 2]. Interestingly, although the gravity term appears as a constant in the conservation of momentum equation, the response of the flow to gravity effect is far from linear. A slight presence of gravity leads to a significant decrease in jet thickness. Indeed, the presence of gravity prohibits the jet from reaching uniform conditions (thickness and velocity) far downstream. In fact, the jet reaches zero thickness at some position downstream, which approximately signals jet breakup. The figure shows that the rate of jet thinning with distance is independent of gravity, although the position for zero (final) thickness is further downstream for lower gravity jets. It can be seen from the figure that beyond a certain value of G, the dependence of the jet thickness on position is uninfluenced by gravity.

Finally, consider the effect of surface tension. Figure 3.6 illustrates the influence of surface tension for We $\in$ [1, 5], Re = 50 and G = 0.5. As seen from the figure, the presence of surface tension tends to prohibit contraction.

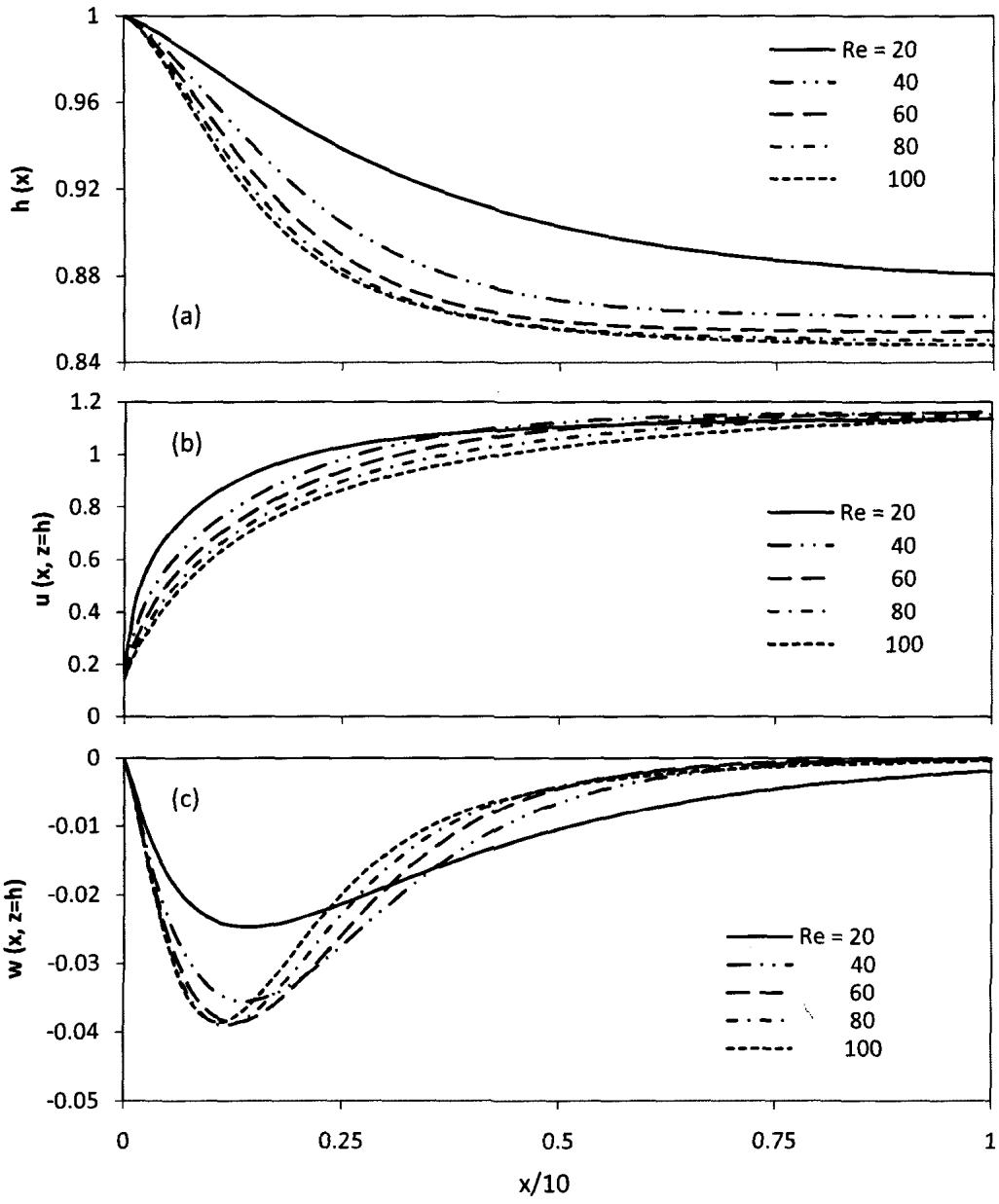

Figure 3.4 Influence of inertia on (a) jet thickness and (b) streamwise velocity and (c) surface transverse velocity in the absence of gravity (G = 0) and in the presence of surface tension (We = 0.5), for Re $\in$ [20, 100].

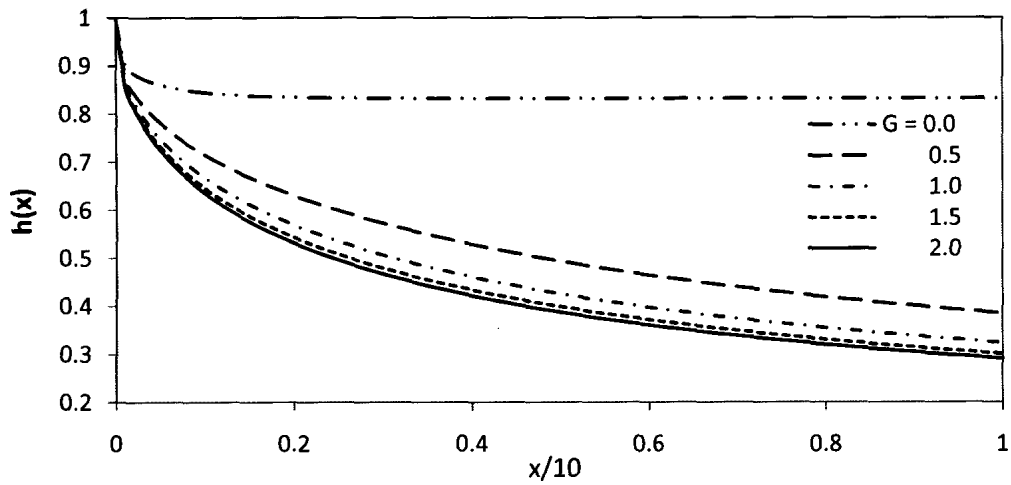

Figure 3.5 Influence of gravity on jet thickness in the absence of surface tension (We = 0), for Re = 50, G ∈ [0, 2].

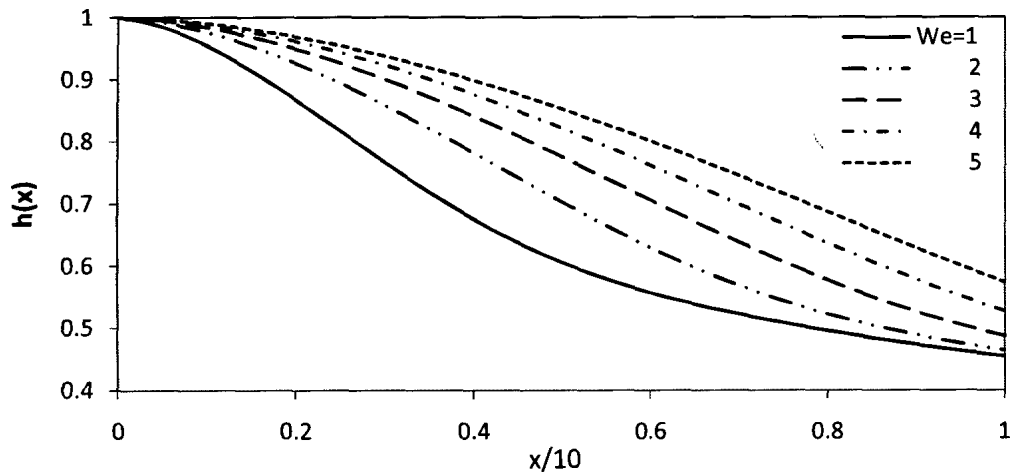

Figure 3.6 Influence of surface tension on jet thickness in the presence of inertia and gravity (Re = 50, G = 0.5) for We ∈ [1, 5].

3.2 Viscoelastic jet flow

After analyzing Newtonian flow, the viscoelastic jet is now taken into account. The effect of inertia, elasticity and surface tension is investigated. The effect of elasticity can be examined by varying either the viscosity ratio or the Deborah number. In the current work, only De is varied and Rv is set equal to 1 (one) unless otherwise specified.

The influence of inertia in the presence of elasticity (De = 1) and surface tension (We = 0.5) is illustrated in Figure 3.7 while the gravity is absent (G = 0). The surface profiles suggest an opposite trend for the flow near and far from the channel exit Inertia tends to enhance contraction near the channel exit, similarly to the Newtonian case (figure 3.4a). Far from the channel exit, the jet reaches a constant thickness, corresponding to the uniform flow as suggested by figure 3.7b, which increase with inertia. For lower Re, the flow travels over a longer distance before it reaches uniform conditions. For a jet with high inertia, the jet exhibits a strong contraction near the exit accompanied by a strong flow of transverse velocity (Figure 3.7c). The position of the minimum in w is, however, not strongly affected by the inertia. At low Re, an overshoot is observed for streamwise velocity but vanishes as Re starts to increase (figure 3.7b). This phenomenon was not observed for the case of a Newtonian fluid. The profiles for the streamwise and transverse normal stress and shear stress components are also displayed in figures 3.7d, 3.7e and 3.7f. As expected, the stresses at the free surface tend to zero eventually far downstream. Interestingly, the relaxation length for the stresses (at least at the free surface) is essentially independent of inertia. The stress profiles indicate a relatively mild overshoot in normal stress and a dip in shear stress at low inertia, where elastic effect tends to be dominant.

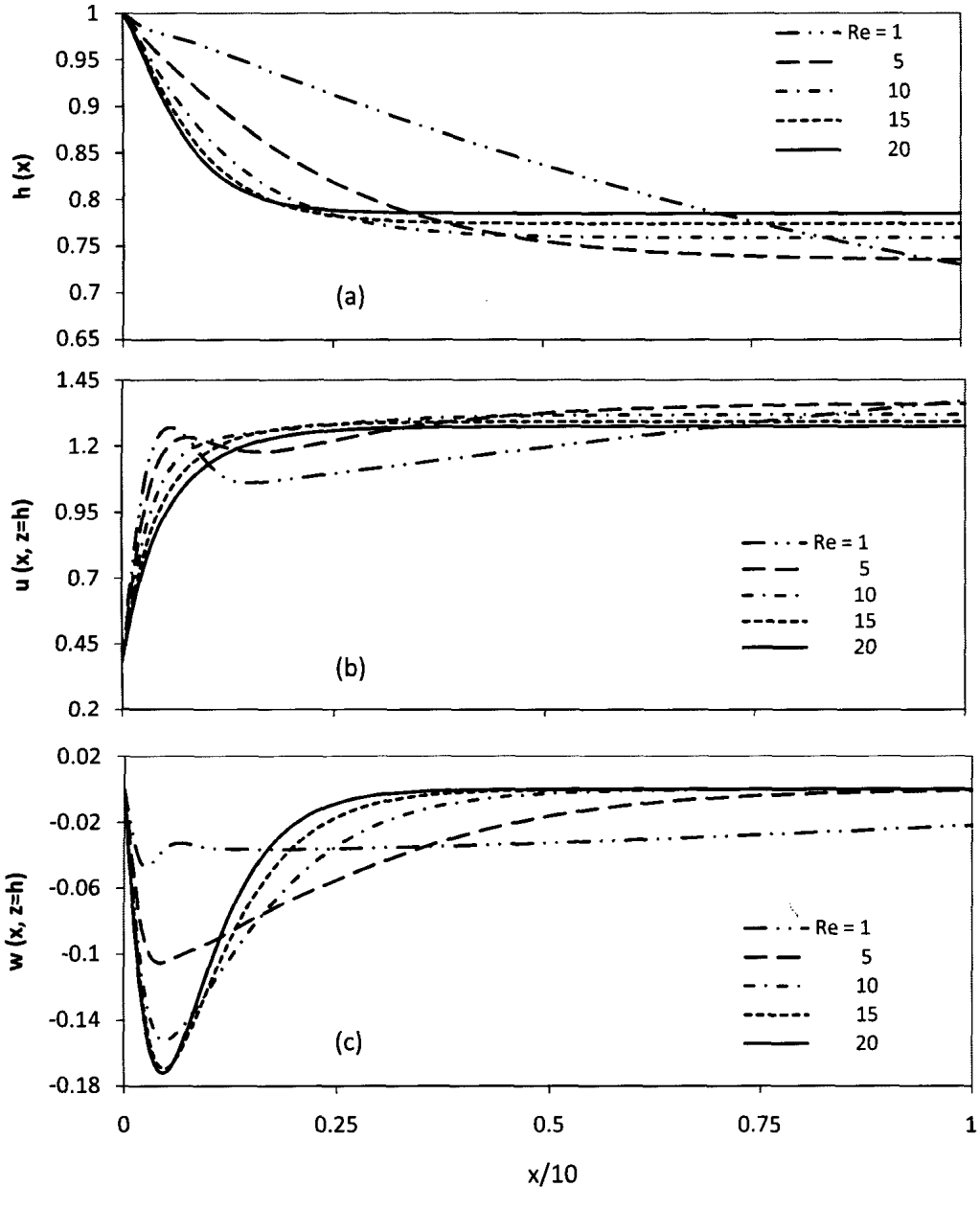
h (x)
1
0.95
0.9
0.85
0.8
0.75
0.7
0.65
(a)
Re = 1
5
10
15
20
u (x, z=h)
1.45
1.2
0.95
0.7
0.45
0.2
(b)
Re = 1
5
10
15
20
w (x, z=h)
0.02
-0.02
-0.06
-0.1
-0.14
-0.18
(c)
Re = 1
5
10
15
20
0
0.25
0.5
0.75
1
x/10

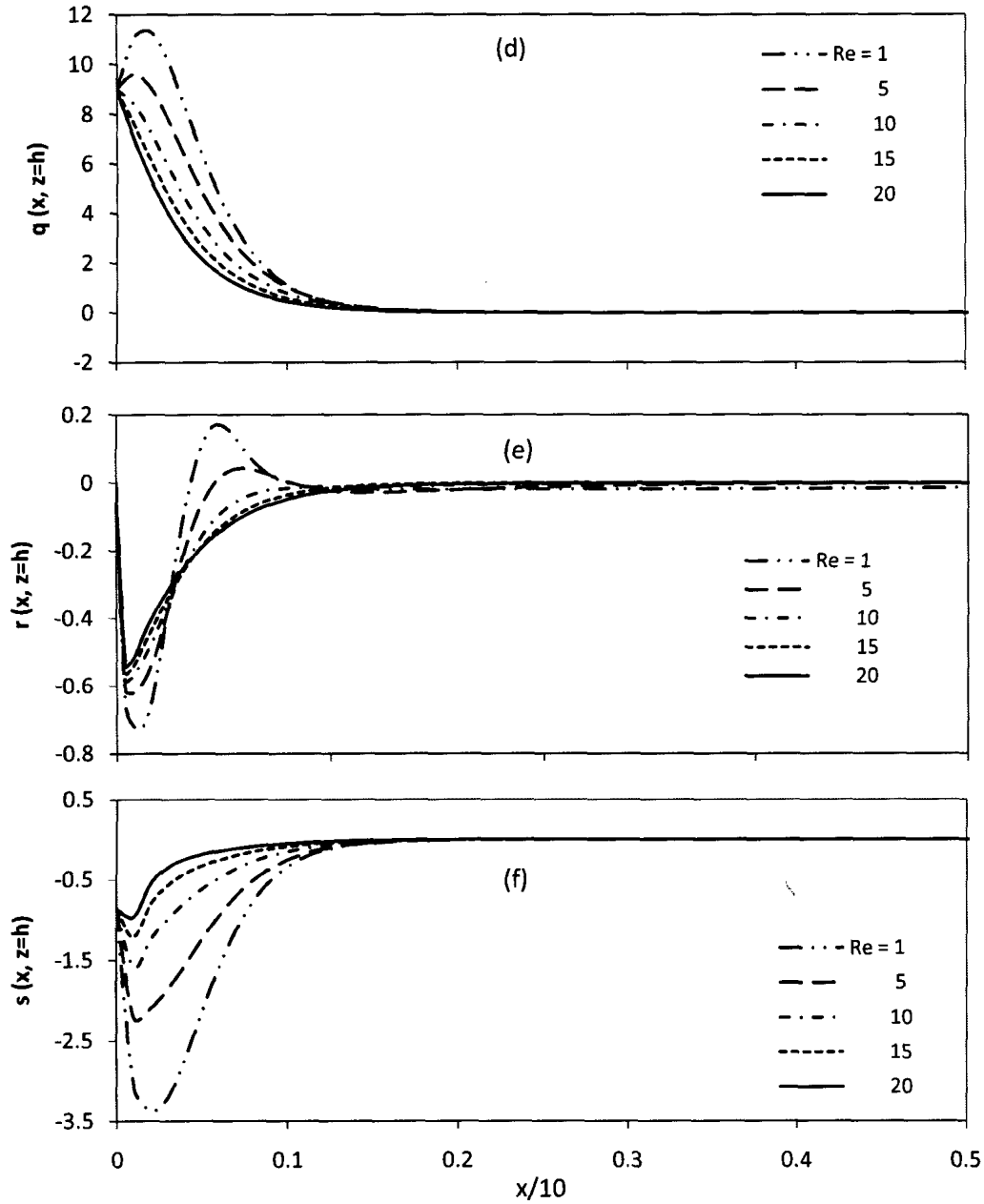

Figure 3.7 Influence of inertia on (a) jet thickness, (b) streamwise velocity, (c) surface transverse velocity, (d) streamwise normal stress, (e) transverse normal stress and (f) shear stress in the absence of gravity (G = 0) and for De = 1 and We = 0.5, Re $\in$ [1,20].

Figure 3.8 displays the influence of elasticity at moderately low Reynolds number (Re = 10) in the absence of gravity and surface tension. The profiles corresponding to the stress components are also included (figure 3.8d – 3.8f). The range of Deborah numbers considered is De $\in$ [1, 5]. Although the De range is relatively small, the flow is strongly influenced by elasticity. For De < 1, the flow is qualitatively of Newtonian character, and will not be shown. Figure 3.8a shows that the level of film contraction near the channel exit is independent of elasticity, but elasticity tends to generally prohibit contraction farther downstream. In fact, jet swelling is found for De >2. For all the cases, the jet thickness reaches a constant level far downstream from the channel exit. In this case, plug flow conditions are reached regardless of the value of De. The jet thickness exhibits a minimum close to the channel exit and levels off further downstream. For the case of a Newtonian fluid, the jet contracts to a constant thickness only. Moreover, a major contrast between Newtonian and viscoelastic jet flow is also reflected. For the Newtonian jet, the flow becomes fully developed and reaches the plug flow condition close to the channel exit. In contrast, a viscoelastic jet displays uniform flow much farther from the channel exit. Figure 3.8c shows that the transverse velocity profiles reflect a strong downward flow just downstream of the thickness minimum location, exhibiting a minimum at a location that is not strongly affected by elasticity. The waviness, which is typically expected for the flow of viscoelastic films, is more evident here from the w than the h profiles. The w profiles exhibit a maximum that accompanies the swell in the jet.

Figure 3.8d, 3.8e and 3.8f show the profiles for the stress components. A significant build-up in streamwise normal stress, q(x, z = h) at the jet surface, with transverse normal stress r (x, z = h) reaching a maximum near channel exit is observed. Stress component figures suggest that the flow tends to be dominated by the elongational (as opposed to shear) effect. The profiles for the polymeric shear stress, s (x, z=h) is displayed in figure 3.8f. Regardless of De, there is an undershoot near the exit but the stress tends to diminish downstream. The transverse velocity profiles show the same trend, except that instead of a maximum value, this shows a minimum (figure 3.8c). Overall, the jet profiles, velocity and normal stress distributions suggest that elasticity tends to play a different role to inertia.

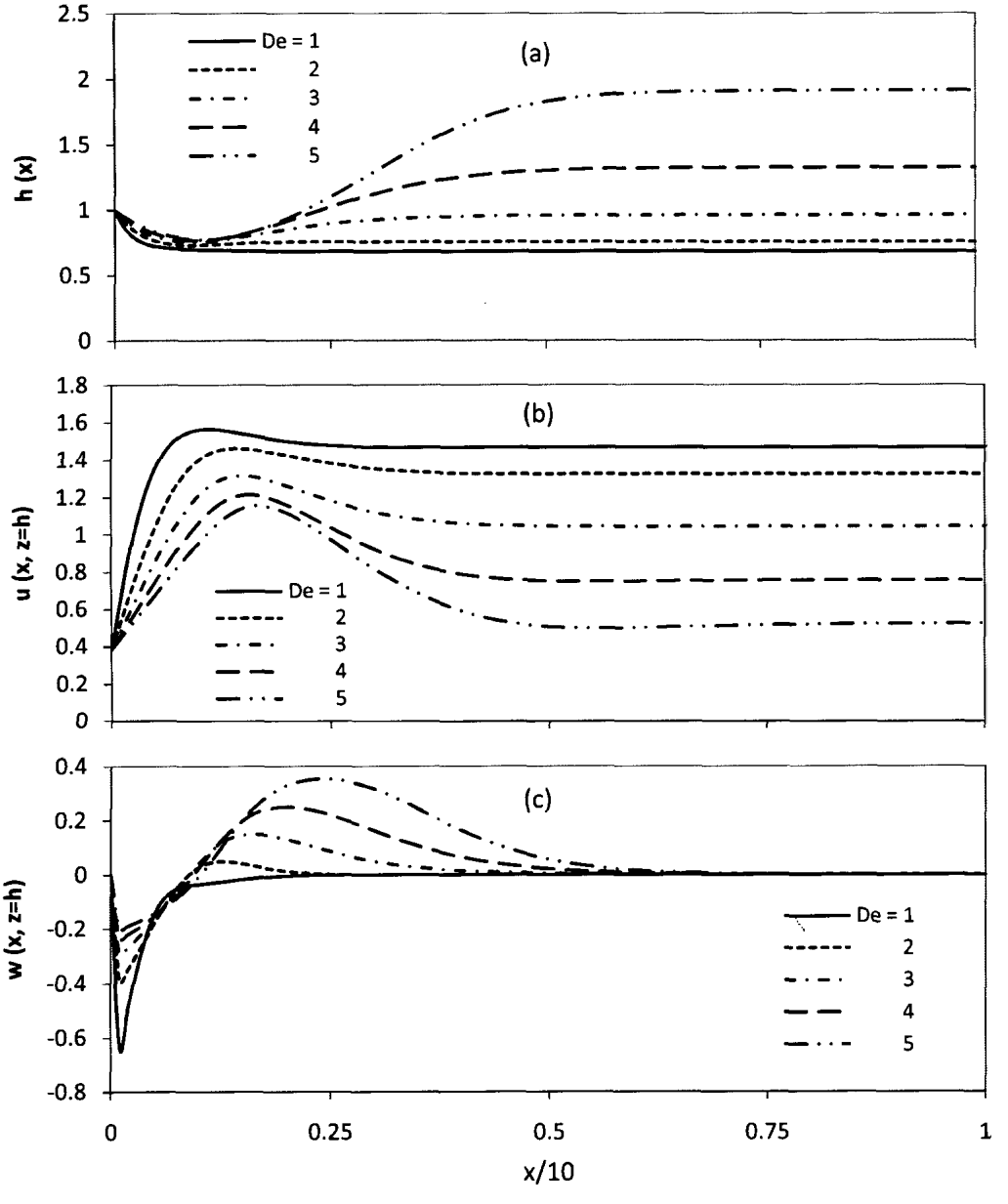
(a)
h (x)
De = 1
2
3
4
5
(b)
u (x, z=h)
(c)
w (x, z=h)
x/10

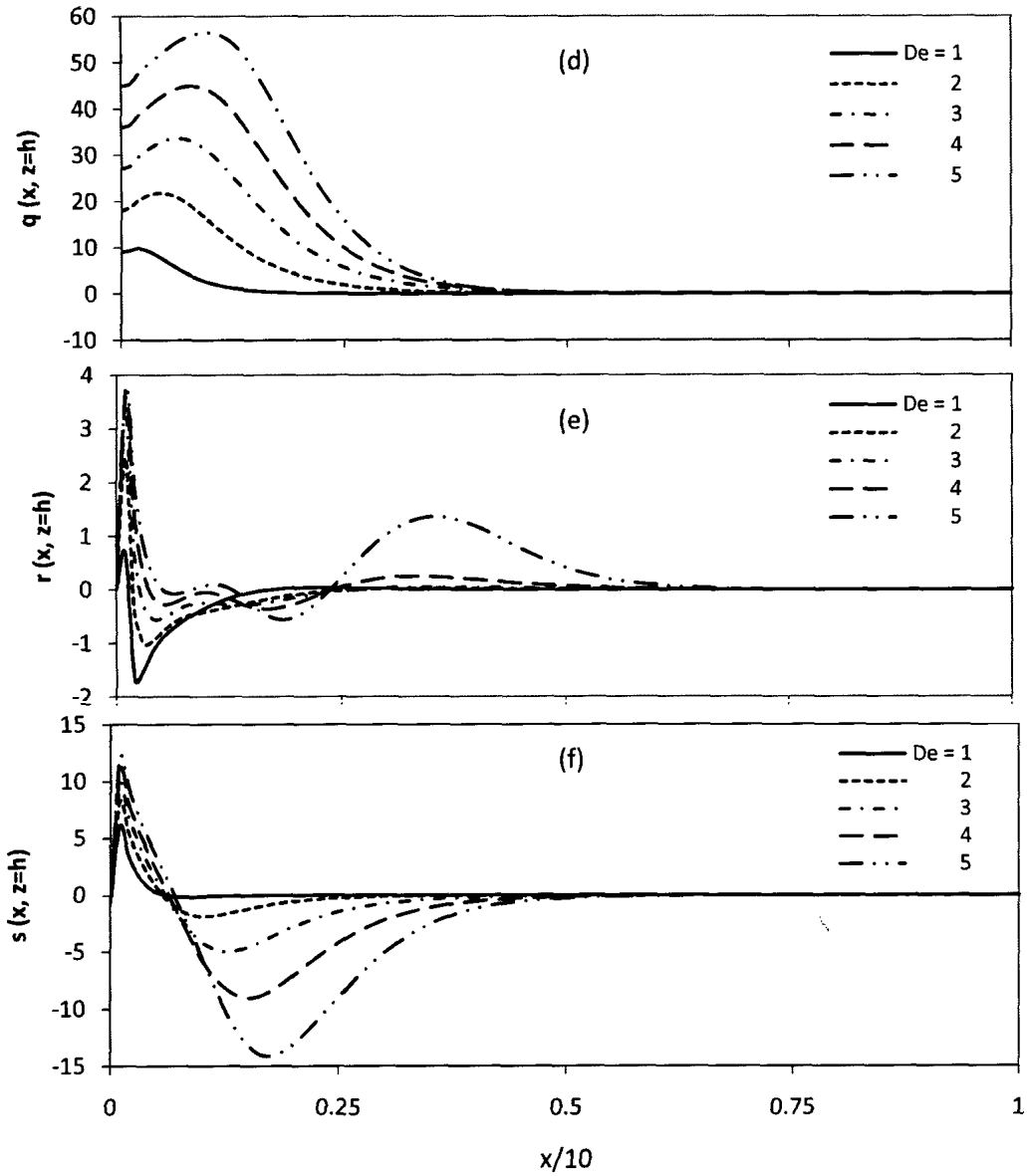

Figure 3.8 Influence of elasticity on (a) jet thickness, (b) streamwise velocity, (c) surface transverse velocity, (d) streamwise normal stress, (e) transverse normal stress, (f) shear stress in the absence of gravity and surface tension (G = We = 0) for Re = 10 and De $\in$ [1, 5].

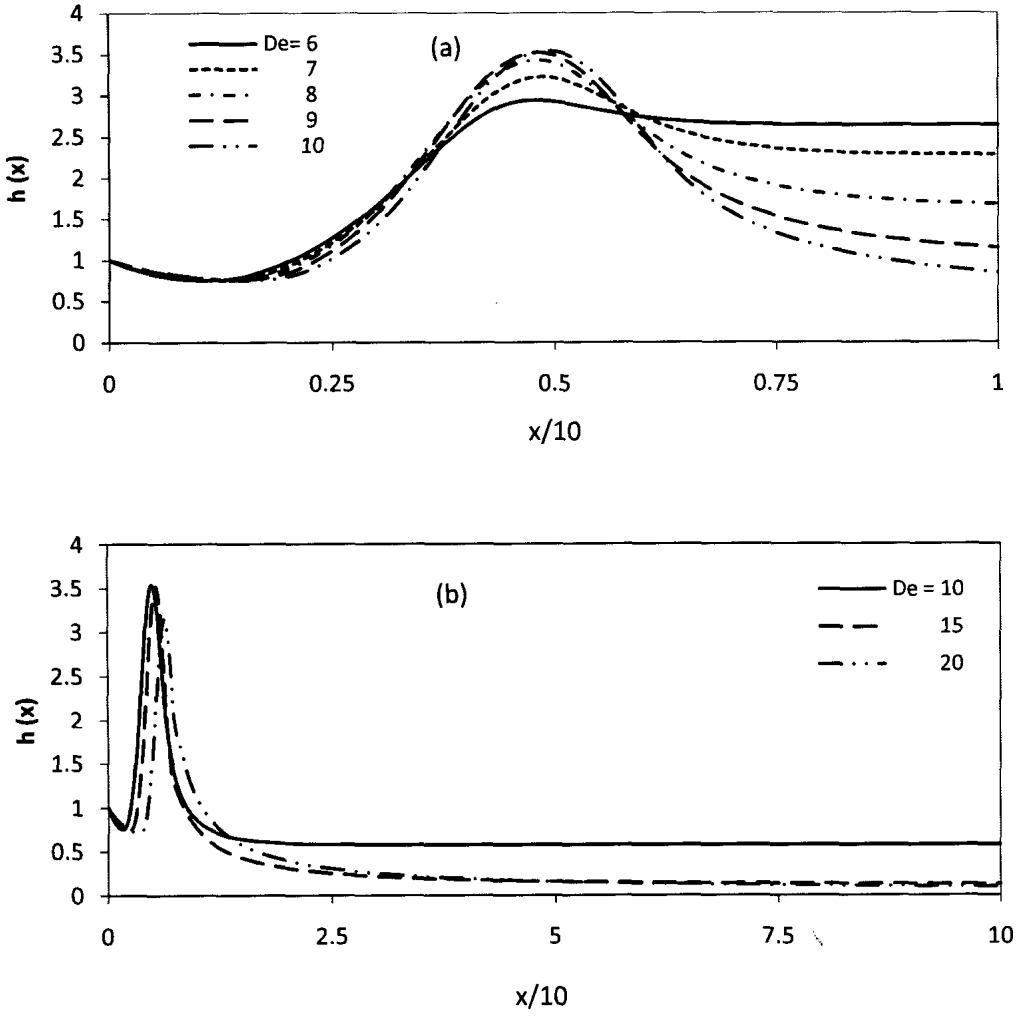

Figure 3.9 Influence of elasticity on (a) jet thickness and (b) swelling in the absence of gravity and surface tension (G = We = 0) for Re = 10.

Beyond a certain value of De (De > 6), the contraction near the channel exit becomes independent of elasticity and the jet shows significant swelling. The profile of the jet shows high swelling as De increases and starts contracting over a shorter distance and eventually reaches a constant thickness (figure 3.9a and 3.9b). In figure 3.9b, the jet profile breaks down (numerically) for high De not very far from the exit. The reason behind this breakdown is the stiffness observed close to the channel exit.

Of close relevance to the present results are the measurements reported by Liang et al. (1999). Although their study focused on the interplay between gravity and normal stress effects, with negligible inertia and axisymmetric flow, some qualitative comparison with the present results is possible. Recall that inertia is always present in the current study, and the Reynolds number, which is based on the driving pressure, is assumed to be of order one. Referring to figure 3.8a, one observes the jet profile reported for a range of De. For small De, the jet contracts right at the channel exit. This is the necking phenomenon, which is typical for a Newtonian jet flow at moderate Re. This behavior was also observed by Liang et al. (1999) in their gray scale images, reproduced here in figure 3.10 for reference and convenience. As De increases, figure 3.8a shows that the jet height near the exit becomes of the same level as the channel height, and for larger De value, the jet has larger diameter than that at the exit. This situation is similar to that reported by Liang et al. (1999) (see figure 3.10b and c).

However, one cannot expect good quantitative agreement for several reasons.

(a) Planar jet flow is considered in the current work while axisymmetric jet flow was examined by Liang et al. (1999).

(b) The current theory is based on the assumption that the jet is thin. This precludes comparison close to the exit where surface curvature is significant. Even further downstream from the exit, experiment shows an increase of local curvature with De (see figure 3.11b). One thus expects the current formulation to break down at large Deborah number.

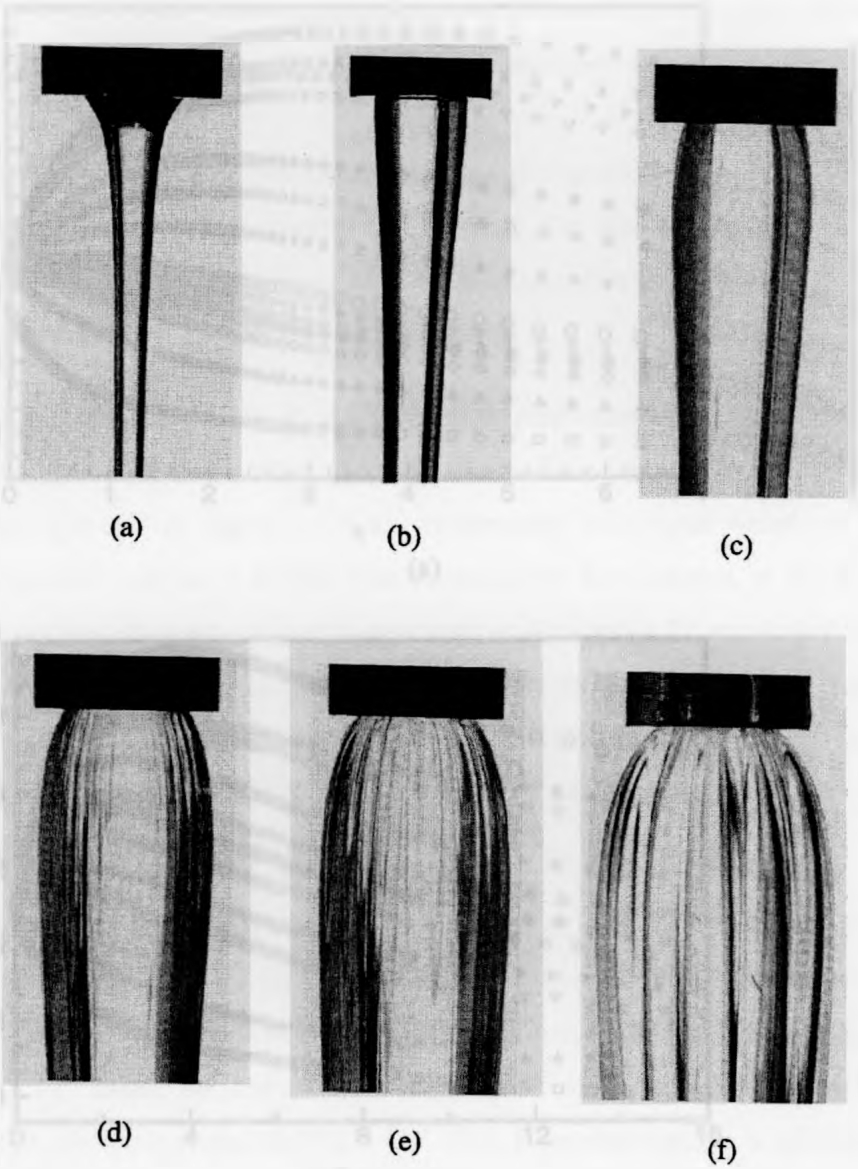

Figure 3.10 Gray-scale images of the viscoelastic jets issuing from a long capillary of radius 4.47 mm. Images shown for different values of Deborah number: (a) 0.12, (b) 0.55, (c) 1.40, (d) 4.08, (f) 9.09, and (g) 15.58. Figure and figure caption reproduced from Liang et al. (1999).

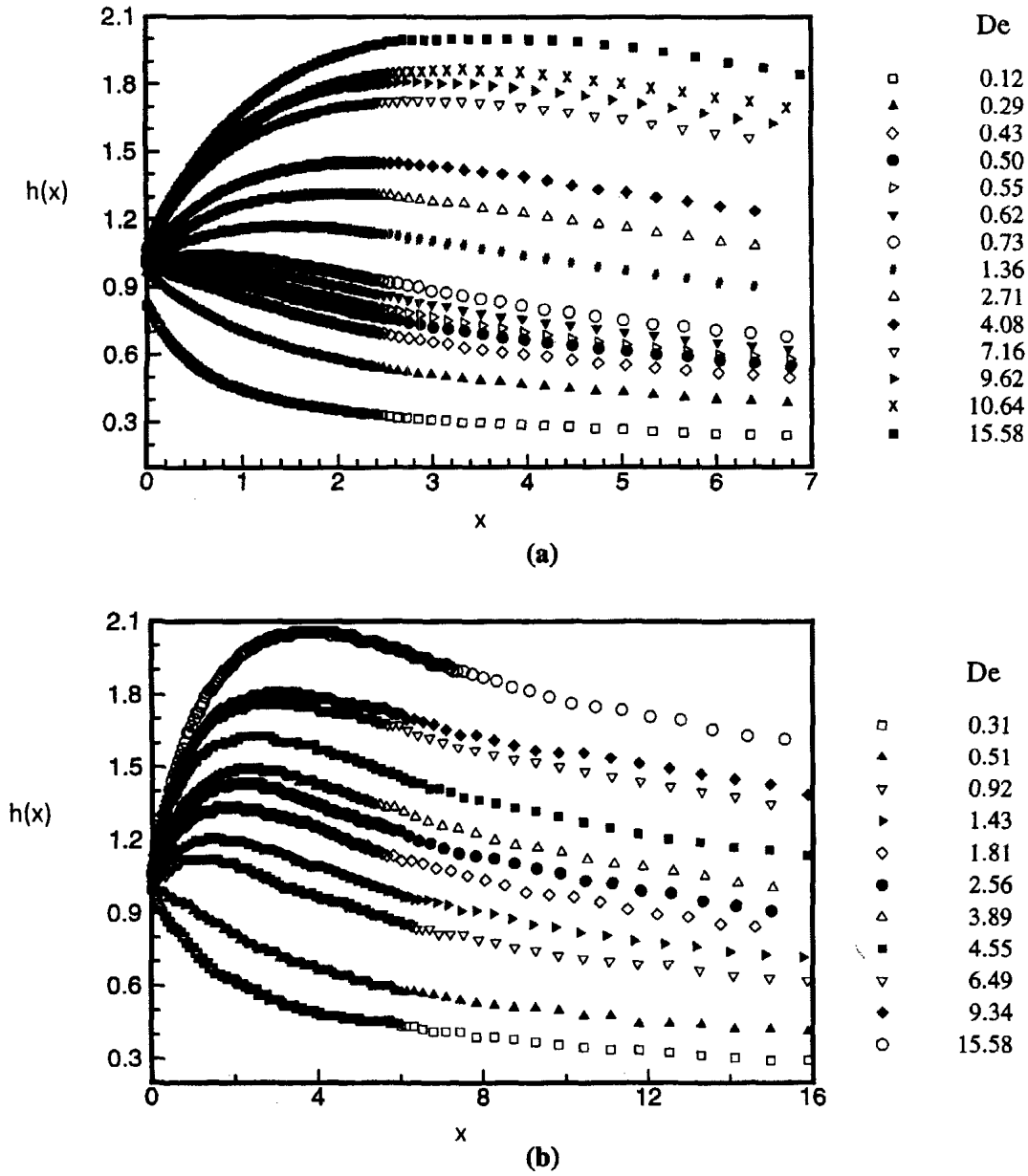

Figure 3.11 Liang et al.'s profiles of the jet plotted as a function of vertical position from the exit at different values of De. Figures reproduced from Liang et al. (1999).

(c) The main driving force in the experiment is gravity. Although gravity can be included in the present calculations, inertia will have to be present as well.

(d) The theory also assumes that the Reynolds number is at least of order one, whereas experimental results are reported for Re ranging 10^{-5} to 10^{-3}. The inclusion of inertia leads to additional contraction that is not reported in the experiment.

Figure 3.11 is taken from Liang et al. (1999) and shows measurements of the jet profiles as function of the Deborah number. Clearly, the profiles close to the exit in figure 3.11a and far from the exit in figure 3.11b are comparable with those based on the current theory as reported in figure 3.8a and 3.9a, respectively. For instance, in the experimental study, the constant thickness of jet far downstream for De= 0.12 was found to be 0.243, and this study predicts the thickness for the same De to be 0.2562. The current jet profiles, however, show the existence of a contraction near the exit that is not present in Liang et al.'s measurements. This discrepancy is of course due to the presence of inertia in the current formulation.

Further comparison between theory and experiment is made by examining the variation of extrudate swell and the position where the maximum swell occurs as function of De. The values for the extrudate swell and its location are, respectively, reported in figures 3.12 and 3.13, based on the current theory and experimental measurements. The theoretical results are reported for Re = 10^{-3}. This Reynolds number is taken deliberately small in an attempt to compare with experiment, although the current theory should preclude, in principle, such small Re value. The theoretical results (figure 3.12a) show that the maximum height remains close to one for De < 2, and increases sharply with Deborah number as De exceeds the critical value of 2, and remains almost unchanged at large values of De. A similar trend is reported by Liang et al. (1999) as shown in figure 3.12b, with De = 0.5 as the critical value for the onset of swell. Results based on Tanner's theory (1970) for the swell ratio are also shown in figure 3.12a. Note that Tanner's theory is based on inertialess flow. In particular, figure 3.12a reflects reasonably close

agreement between the two theories in the smaller De range. Comparison between Liang et al.'s experiment and Tanner's formula for axisymmetric flow also shows agreement in the small De range only. Both the current theory and experiment reflect the lack of validity of Tanner's theory for large De. Some background on Tanner's theory is given next.

Tanner's formula, which predicts the extrudate swell ratio for planar flow, is given in terms of the primary normal stress difference and shear stress ratio at the wall as

$$h_{max} = \left(1 + \frac{1}{12}\left(\frac{N_1}{\Sigma_{xz}}\right)^2_{wall}\right)^{\frac{1}{4}} \tag{3.1}$$

This expression can be cast in terms of dimensionless parameters for the present purpose. Indeed, recall the expressions for the stress components from section 2.1.1, which are re-written in terms of the mean velocity in the channel.

In this case, the stress components at the wall become

$$\Sigma_{XZ} = -\frac{\mu D}{2\mu}\frac{dP}{dX} = 6\frac{\mu U_0}{D} \tag{3.2a}$$

$$\Sigma_{XX} = \frac{\lambda\mu_p}{2\mu^2}\left(\frac{dP}{dX}D\right)^2 = \frac{\lambda\mu_p D^2}{2}\left(12\frac{U_0}{D^2}\right)^2 = \frac{72\lambda\mu_p U_0^2}{D^2} \tag{3.2b}$$

Upon noting from (3.2) that

$$\frac{N_1}{\Sigma_{xz}} = \frac{72\lambda\mu_P U_0^2}{D^2} / 6\frac{\mu U_0}{D} = \frac{12\mu_p\lambda U_0}{\mu D} = 6\frac{\lambda U_0}{H_0}\frac{\mu_p}{\mu} \tag{3.3}$$

and inserting (3.3) into (3.1), one obtains

$$h_{max} = \left(1 + 3a^2 De^2\right)^{\frac{1}{4}} \tag{3.4}$$

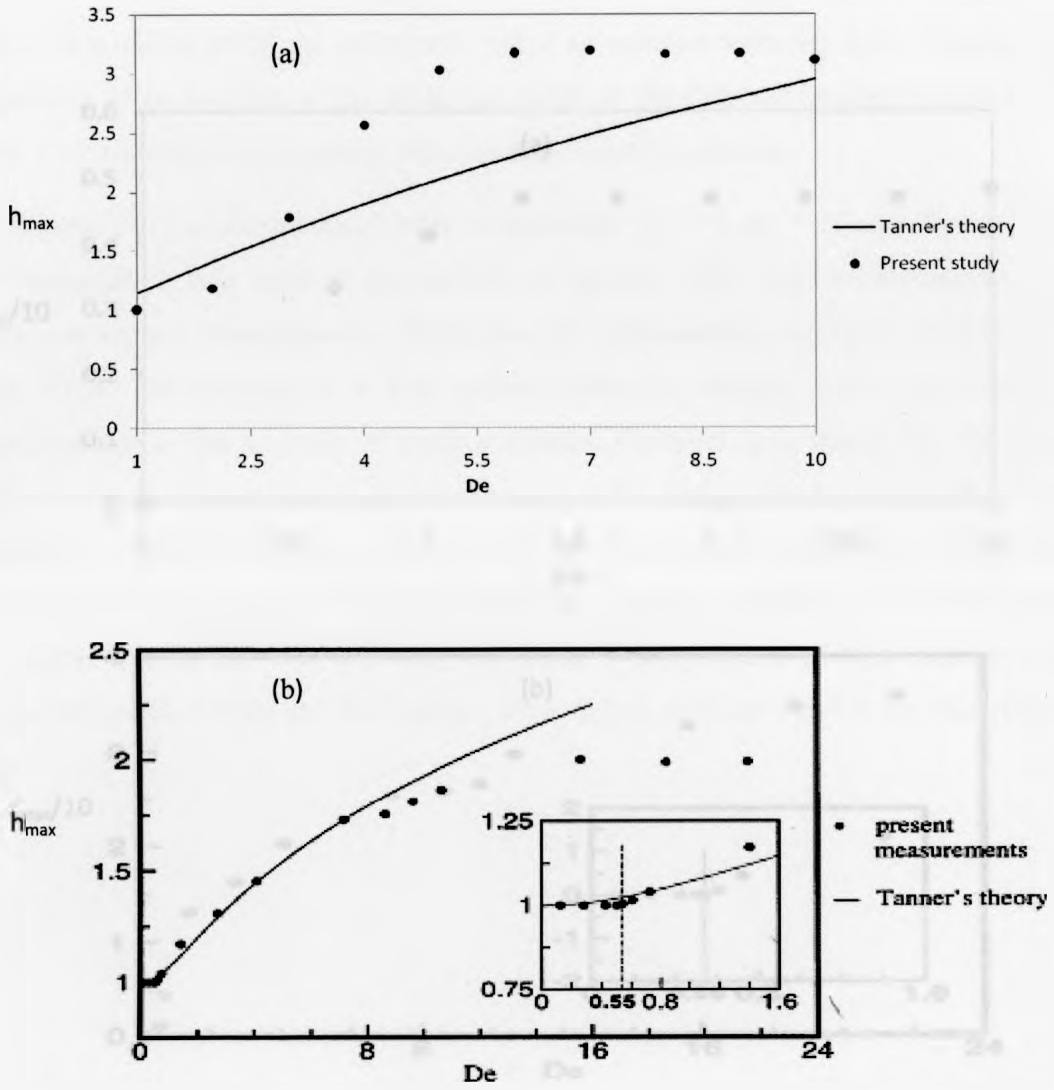

Figure 3.12 The maximum jet thickness as a function of De from (a) present study and (b) experimental results from Liang et al. (1999). Tanner's formulas are also added as solid lines for planar (a) and axisymmetric (b) flows.

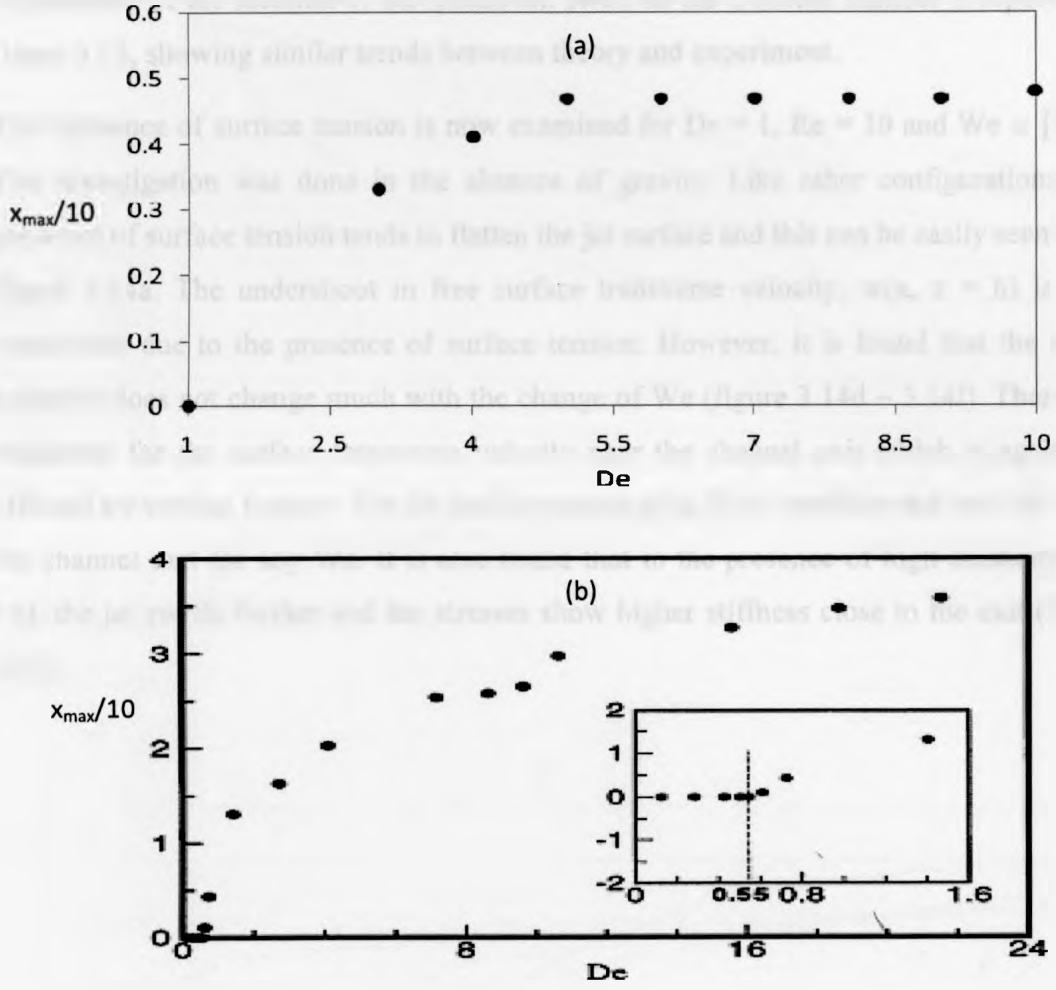

Figure 3.13 The position of maximum swell as a function of De from (a) current study and (b) experimental results from Liang et al. (1999).

Here, a is recalled to be the polymeric solute to solution viscosity ratio. Finally, the dependence of the location of the maximum swell on the Deborah number is reported in figure 3.13, showing similar trends between theory and experiment.

The influence of surface tension is now examined for De = 1, Re = 10 and We $\in$ [1, 5]. The investigation was done in the absence of gravity. Like other configurations, the presence of surface tension tends to flatten the jet surface and this can be easily seen from figure 3.14a. The undershoot in free surface transverse velocity, w(x, z = h) is also minimized due to the presence of surface tension. However, it is found that the stress behavior does not change much with the change of We (figure 3.14d – 3.14f). There is a minimum for the surface transverse velocity near the channel exit which is again not affected by surface tension. The jet profile reaches plug flow condition not very far from the channel exit for any We. It is also found that in the presence of high elasticity (De >5), the jet swells further and the stresses show higher stiffness close to the exit (figure 3.15).

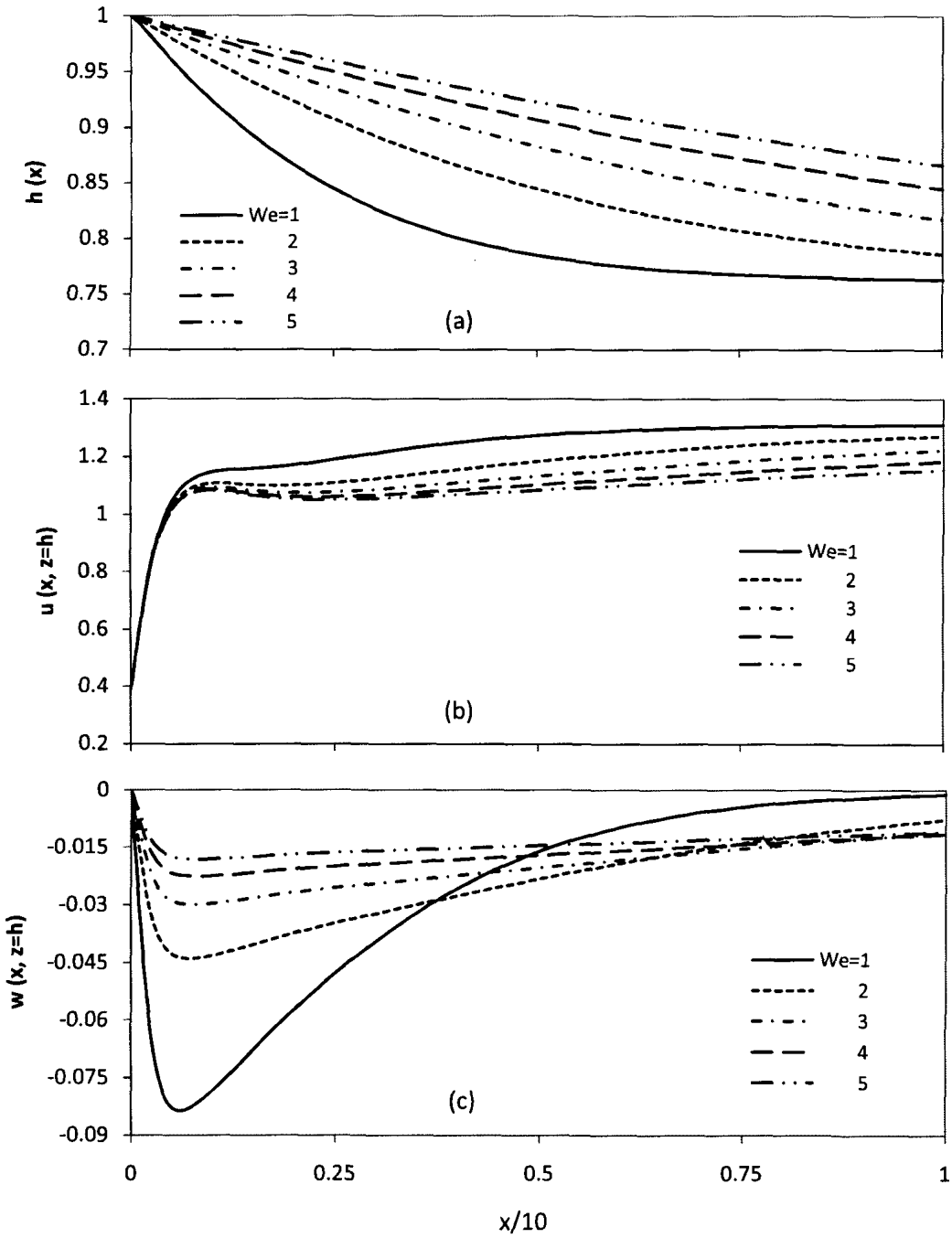
h (x)
1
0.95
0.9
0.85
0.8
0.75
0.7
We=1
2
3
4
5
(a)
u (x, z=h)
1.4
1.2
1
0.8
0.6
0.4
0.2
We=1
2
3
4
5
(b)
w (x, z=h)
0
-0.015
-0.03
-0.045
-0.06
-0.075
-0.09
We=1
2
3
4
5
(c)
0
0.25
0.5
0.75
1
x/10

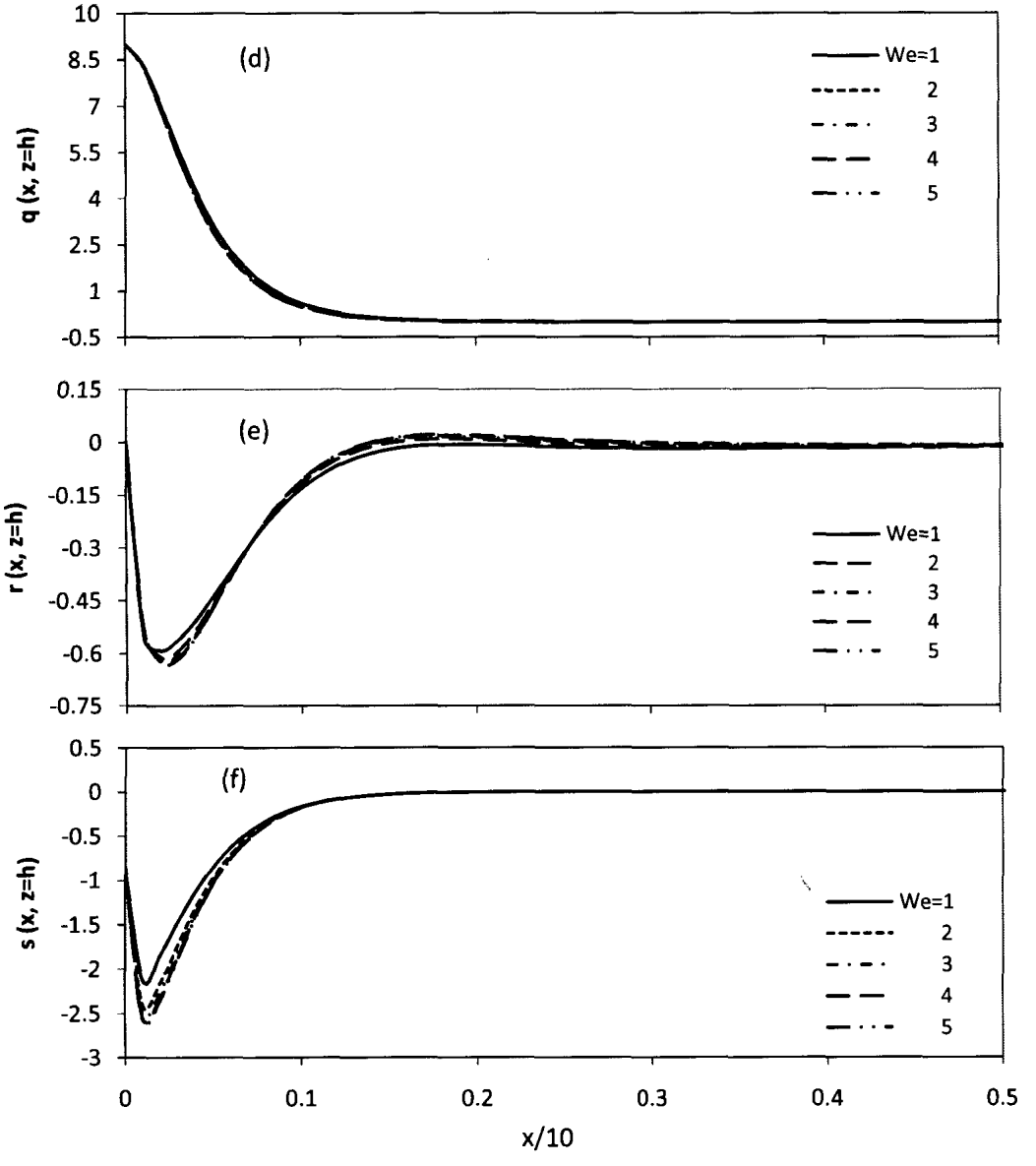

Figure 3.14 Influence of surface tension on (a) jet thickness, (b) streamwise velocity, (c) surface transverse velocity, (d) streamwise normal stress, (e) transverse normal stress and (f) shear stress in the absence of gravity (G = 0) for Re = 10 and De = 1, We $\in$ [1, 5].

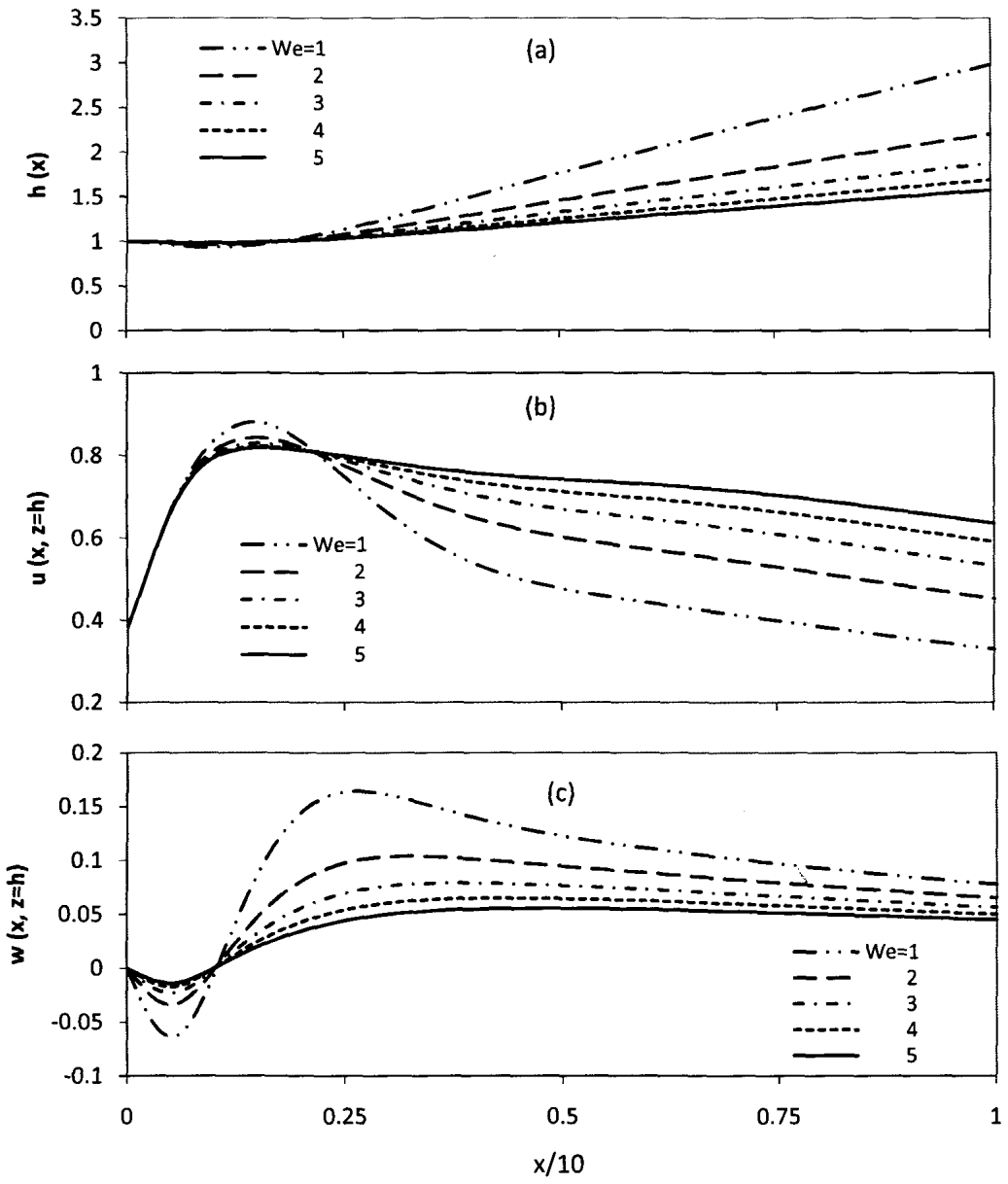
(a)
We=1
2
3
4
5
h (x)
3.5
3
2.5
2
1.5
1
0.5
0
(b)
u (x, z=h)
1
0.8
0.6
0.4
0.2
(c)
w (x, z=h)
0.2
0.15
0.1
0.05
0
-0.05
-0.1
0
0.25
0.5
0.75
1
x/10

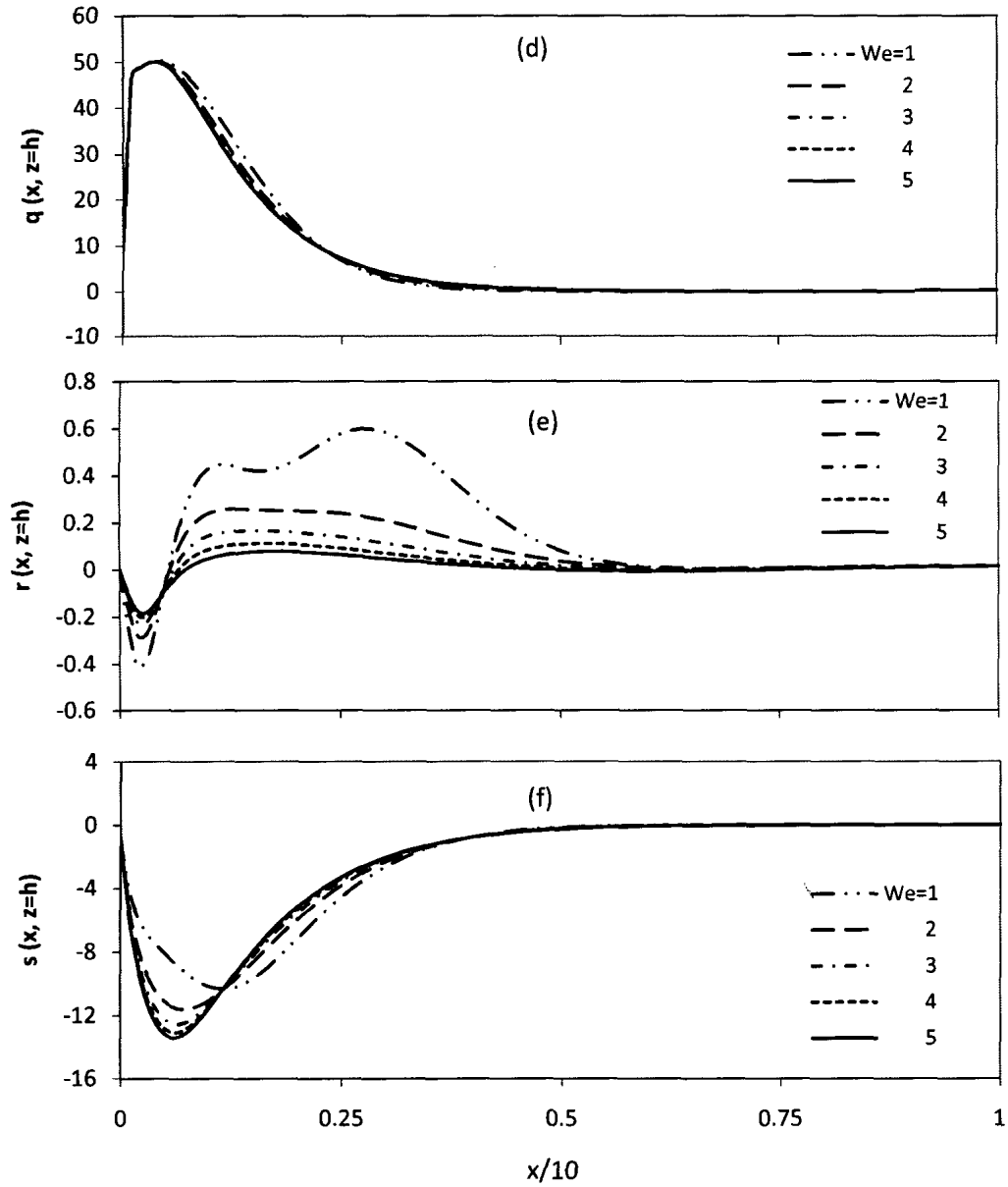

Figure 3.15 Influence of surface tension on (a) jet thickness, (b) streamwise velocity, (c) surface transverse velocity, (d) streamwise normal stress, (e) transverse normal stress and (f) shear stress in the absence of gravity (G = 0) for Re = 10 and De = 5, We $\in$ [1, 5].

CHAPTER 4

CONCLUSION

4.1 Concluding remarks and summary

The symmetric two-dimensional flow of a thin viscoelastic fluid jet emerging from a vertical channel is examined in this study. The fluid is assumed to be a polymeric solution comprising a Newtonian solvent and a polymeric solute, modeled following the Oldroyd-B constitutive equation. The problem is of direct relevance to polymeric processes such as high speed extrusion, film casting and fiber spinning where inertia can play a significant role, but has been widely ignored in previous studies. The influence of inertia, elasticity and gravity on the profiles of velocity and stress components in the presence of surface tension is investigated for steady flow only. The thin-film equations are derived following the scaling of boundary-layer theory, and are solved by expanding the flow field and stresses in terms of orthonormal modes in the transverse direction using the Galerkin projection. In contrast to the depth-averaging technique, the proposed method predicts the shape of the free surface, as well as the velocity and stress components within the fluid.

For a Newtonian jet, the jet thickness remains essentially constant with x for large Reynolds number. However, the flow is strongly dependent on inertia for small Reynolds number with the jet tending to contract and collapse onto a thin line as Re approaches 0. The thickness for a Newtonian jet was shown to vary only monotonically, whereas a viscoelastic jet tends to thicken downstream of the channel exit. Steady Newtonian jet flow becomes fully developed only far downstream from the channel exit. The profile for jet thickness shows an opposite trend in the presence of surface tension to that in the absence of surface tension. In this case, inertia tends to strengthen the contraction. The response of the flow to gravity effect is far from linear. A slight presence of gravity leads to a significant decrease in jet thickness. Finally, due to presence of surface tension, the contraction is prohibited.

It was found that inertia affects significantly the flow of a viscoelastic fluid. The jet tends to reach constant thickness at a relatively short distance with inertia. This contraction of jet surface height near the exit is followed by strong downward flow of surface transverse velocity. At low Re, an overshoot was observed for streamwise velocity profile which vanishes with the increase of Re. This phenomenon was not observed for the case of a Newtonian fluid. The stress components show a jump near the channel exit, but eventually tend to relax far downstream.

The elastic effect is found to be more influential near the channel exit. For a relatively small range of De, the flow shows significant changes. The jet profile tends to show swelling as De increases. In contrast to the Newtonian flow, viscoelastic flow reaches plug flow condition much farther from the channel exit. A sharp gain is predicted for the streamwise normal stress component, q and transverse normal stress component, r close to the channel exit. The shear stress component, s shows an overshoot but monotonically decreases to zero height. A saturation effect for large De was observed, suggesting a stress relaxation at a short distance. From the stress component figures, it can be suggested that the flow will be dominated by the elongational effect as opposed to shear. Overall, the profiles suggest that elasticity tends to play a different role to inertia. Investigation on the effect of surface tension suggests that the viscoelastic jet surface tends to flatten in the presence of surface tension similar to the Newtonian jet. However, the stress components are not affected much by the change of surface tension. Finally, comparison with the experiment of Liang et al. (1999) for axisymmetric jet as well as with Tanner's theory for planar jet leads to good qualitative agreement.

4.2 Future work

The current work has done as an initial step towards the study of viscoelastic fluid flow with moderately high inertia. As an expansion to the current work, the following can be done.

(a) Jet flow of a viscoelastic fluid emerging from a two-dimensional vertical channel was investigated in this study with the aid of the weighted residual method. Other flow configurations such as coating flow (wall jet), axisymmetric jet and even entry flow of a viscoelastic fluid can be examined using the same method.

(b) In this work, viscoelastic constitutive equation adopted corresponded to an Oldroyd-B fluid which provides a quite simple viscoelastic model for dilute polymer solutions. However, more robust, accurate and realistic constitutive models such as Phan-Thien Tanner (Phan-Thien and Tanner 1977), White-Metzner (White, Metzner and Denn 1966) and other more complicated models can be employed in the future.

(c) Only steady flow of a jet is considered in this work, but it can be extended to analyze the transient flow. Also, the thermal behavior of the jet can be investigated.

(d) A stability analysis can be done to examine the stability of the steady states computed in this thesis.

Bibliography

ALEKSEENKO, S. V., NAKORYAKOV, V. E., POKUSAEV, B. G. 1985, Wave formation on a vertical falling liquid film, *AIChE J.* **31**: 1446.

AGASSANT, J, F., AVENAS, P., SERGENT, J. P. H., CARREAU P. J. 1986, *Polymer Processing: Principle and Modelling,* Hanser.

BENNEY, D. J. 1966, Long waves in liquid films, *J. Math, Phys.* **45**: 150.

BÉRDAUDO, C., FORTIN, A., COUPEZ, T., DEMAY, Y., VERGNES, B., AGASSANT, J.F. 1998, A finite element method for computing the flow of multi-mode viscoelastic fluids: comparison with experiments, *J. Non-Newtonian Fluid Mech.* **75**: 1.

BERTSCHY, J. R., CHIN, R. W. & ABERNATHY, F. H. 1993, High-strain-rate free-surface boundary-layer flows, *J. Fluid Mech.* **216**: 443.

BIRD, R. B., ARMSTRONG, R. C. & HASSANGER, O. 1987, *Dynamics of polymeric liquids*, vol. 1, 2nd edn., JohnWiley.

BOUSFIELD, D. W., KEUNINGS, R., MARRUCCI, G. & DENN, M. M. 1986, Non-linear analysis of the surface tension driven breakup of viscoelastic filaments, *J. Non-Newtonian Fluid Mech.* **21**: 79.

BROUSSEAU, P. 1990, Ph.D. Dissertation.

BUSH, M. B. 1990, A numerical study of extrudate swell in dilute polymer solutions represented by the Oldroyd-B model, *J. Non-Newtonian Fluid Mech.* **34**: 15.

CHAI, M. S., YEOW, Y. L. 1988, Modelling of Boger fluid jets using the Oldroyd-B equation- a comparison of experimental and numerical results, *J. Non-Newtonian Fluid Mech.* **29**: 433.

CHANG, H. C., DEMEKHIN, E. A., KOPELEVICH, D.I. 1993, Non-linear evolution of waves on a falling film, *J. Fluid Mech.* **250**: 433.

CHANG, H. C. 1994, Wave evolution on a falling film, *Ann. Rev. Fluid Mech.* **26**: 103.

CHANG, J. C., DENN, M. M. 1979, An experimental study of isothermal spinning of a Newtonian and a viscoelastic liquid, *J. Non-Newtonian Fluid Mech.* **5**: 369.

CHRISTANTI, Y. & WALKER, L. M. 2001, Surface driven jet break up of strain hardening polymer solutions, *J. Non-Newtonian Fluid Mech.* **100**: 9.

CROCHET, M. J., KEUNINGS, R. 1982, Finite element analysis of die swell of a highly elastic fluid, *J. Non-Newtonian Fluid Mech.* **10**: 339

DEMEKHIN, E. A., SHKADOV, V. YA. 1985, Two-dimensional wave regimes of a thin liquid film, *Izv. Akad. Nauk SSSR, Mekh. Zhidk. Gaza* **3**: 63.

DONNELLY, G. J., WEINBERGER, C. B. 1975, Stability of isothermal fiber spinning of a Newtonian fluid, *Ind. Eng. Chem. Fund.* **14** (4), 334–337.

DOUFAS, A., MCHUGH, A., MILLER, C. 2000, Simulation of melt spinning including flow-induced crystallization. Part I. Model development and predictions, *J. Non-Newtonian Fluid. Mech.* **92**, 27–66.

FRENKEL, A. L. 1992, Non-linear theory of strongly undulating thin films flowing down vertical surfaces, *Europhys, Letts.* **18**: 583.

GAIDOS, R. E., DARBY, R. 1988, Numerical simulation and change in type in the developing flow of a non-linear viscoelastic fluid, *J. Non-Newtonian Fluid Mech.* **29**: 59.

GANVIR, V., LELE, A., THAOKAR, R., GAUTHAM, B. P. 2007, Simulations of viscoelastic flows of polymer solutions in abrupt contractions using an arbitrary Lagrangian Eulerian (ALE) based finite element method, *J. Non-Newtonian Fluid Mech.* **143**: 157.

GERMAN, R., KHAYAT, R. E. 2005, Steady and transient thin-jet flow, *Phys. Fluids* **17**:102104.

GOREN, S. L., WRONSKI, S. 1966, The shape of low speed capillary jets of Newtonian liquids, *J. Fluid Mech.* **25**: 185.

KARAPESTAS, G., TSAMOPOULOS, J. 2008, Steady extrusion of viscoelastic materials from an annular die, *J. Non-Newtonian Fluid Mech.* **154**: 136.

KANG, F., CHEN, K.P. 1995, Non-linear elastic instability of gravity-driven flow of a thin viscoelastic film down an inclined plane, *J. Non-Newtonian Fluid Mech.* **57**: 243.

KESHTIBAN, I. J., BELBLIDIA, F., WEBSTER, M. F. 2004, *J. Non-Newtonian Fluid Mech.* **122**: 131.

KHAYAT, R. E. 2001, Transient two-dimensional coating flow of a viscoelastic fluid film on a substrate of arbitrary shape, *J. Non-Newtonian Fluid Mech.* **95**: 199.

KHAYAT, R. E., WELKE, S. 2001, Influence of inertia, gravity and substrate topography on the two-dimensional transient coating flow of a thin Newtonian fluid film, *Phys. Fluids* **13**: 355.

KHAYAT, R. E., KIM, K. 2002, Influence of initial conditions on transient two-dimensional thin-film flow, *Phys. Fluids* **14**: 4448.

KHAYAT, R. E., KIM, K. 2006, Thin-film flow of a viscoelastic fluid on an axisymmetric substrate of arbitrary shape, *J. Fluid Mech.* **552**:31.

KIM, K. & KHAYAT, R. E. 2002, Influence of non-Newtonian effects on the transient flow of a thin fluid film, *Phys. Fluids* **14**: 2202.

KIRIAKIDIS, D. G., PARK, H. J., MITSOULIS, E., VERGNES, B., AGASSANT, J. F. 1993, A study of stress distribution in contraction flows of an LLDPE melt, *J. Non-Newtonian Fluid Mech.* **47**: 339.

KRIEGSMANN, J. J., MIKIS, M. J., VANDEN-BROEK, J. 1998, Pressure driven disturbances on a thin viscous film, *Phys. Fluids* **10**: 1249.

LIANG, Y., OZTEKIN, A., NETI, S. 1999, Dynamics of viscoelastic jets of polymeric liquid extrudate, *J. Non-Newt. Fluid Mech.* **81:** 105.

MIDDLEMAN, S. 1977, *Fundamentals of Polymer Processing*, McGraw-Hill.

MISSIRLIS, K. A., ASSIMACOPOULOS, D., MITSOULIS, E. 1998, A finite volume approach in the simulation of viscoelastic expansion flows, *J. Non-Newtonian Fluid Mech.* **78**: 91.

MITSOULIS, E. 2010, Extrudate swell of Boger fluids, *J. Non-Newtonian Fluid Mech.* **165**: 812.

OOSHIDA, T. 1999, Surface equation of falling film flows with moderate Reynolds number and large but finite Weber number, *Phys. Fluids* **11**: 3247.

OSSWALD, T., HERNANDEZ-ORTIZ, J. 2006, *Polymer Processing: Modelling and Simulation*, 1st edn., Hanser.

PHILLIPS, T. N., WILLIAMS, A. J. 1999, Viscoelastic flow through a planar contraction using a semi-Lagrangian finite volume method, *J. Non-Newtonian Fluid Mech.* **87**: 215.

POOLE, R. J., ALVES, M. A., OLIVEIRA, P. J., PINHO, F. T. 2007, Plane sudden expansion flows of viscoelastic liquids, *J. Non-Newtonian Fluid Mech.* **146**: 79.

PROKOPIOU, T., CHENG, M. & CHANG, H. C. 1991, Long waves on inclined films at high Reynolds, *J. Fluid Mech.* **222**: 665.

ROBERT, K. P., GREGORY, G. W. 1994, Elongational flow of solutions of rodlike micelles, *Langmuir* **10**, 3419-3426.

RODD, L. E., LEE, D., AHN, K. H., COOPOER-WHITE, J. J. 2010, The importance of downstream events in microfluidic viscoelastic entry flows: Consequences of increasing the constriction length, *J. Non-Newtonian Fluid Mech.* **165**: 1189.

RUYER-QUIL, C., MANNEVILLE, P. 1998, Modeling film flows down inclined planes, *Eur. J. Phys.* **6**: 277.

SHKADOV, V. Y. 1967, Wave conditions of a flow in a thin viscous layer under the action of gravitational forces, *Izv. Akad. Nauk. SSSR Mehk, Zhid. Gaza* **1:** 43.

TANNER, R.I. 2000, *Engineering Rheology*, 2nd edn., Oxford Univ. Press.

TANNER, R. I., BUSH, M. B., PHAN-THIEN, N. 1985, A boundary element

investigation of extrudate swell, *J. Non-Newtonian Fluid Mech.* **18**: 143.

TAUQEER MUHAMMAD, KHAYAT, R. E. 2004, Effect of substrate movement on shock formation in pressure-driven coating flow, *Phys. Fluids* **16**: 1818

TOME, M. F., DUFFY, B., MCKEE, S. 1996, A numerical technique for solving non-Newtonian free surface flow, *J. Non-Newtonian Fluid Mech.* **62**: 9.

TOME, M. F., CASTELO, A., FERREIRA, V. G., MCKEE, S. 2008, A finite difference technique for solving the Oldroyd-B model for 3D-unsteady free surface flows, *J. Non-Newtonian Fluid Mech.* **154**: 179.

TOME, M. F., PAULO, G. S., PINHO, F. T., ALVES, M. A. 2010, Numerical solution of the PTT constitutive equation for unsteady three-dimensional free surface flows, *J. Non-Newtonian Fluid Mech.* **165**: 247.

TRANG-CONG, T., PHAN-THIEN, N. 1988, Three-dimensional study of extrusion processes by boundary-element method. II. Extrusion of a viscoelastic fluid, *Rheol. Acta* **27**: 639.

TRIVFONOV, YU., TSVELODU, O., YU. 1991, Non-linear waves on the surface of a falling liquid film part I, *J. Fluid Mech.* **229**: 531.

WATSON, E. J., 1964, The radial spread of a liquid jet over a horizontal plane, *J. Fluid Mech.* **20**: 217.

WILKES, J. O., NEDDERMAN, R. M. 1962, The measurement of velocities in thin film of liquid, *Chem. Eng. Sci.* **17**: 177.

YUAN, X. F., BALL, R. C., EDWARDS, S. F. 1994, Dynamical modelling of viscoelastic extrusion flows, *J. Non-Newtonian Fluid Mech.* **54**: 423

ZHANG, Y. L., MATAR, O. K., CRASTER, R. V. 2002, Surfactant spreading on a thin weakly viscoelastic film, *J. Non-Newtonian Fluid Mech.* **105**: 53.

ZIENKIEVICZ, O. C., HEINRICH, J. C. 1979, A unified treatment of steady-state shallow water and two-dimensional Navier–Stokes equations: finite-element penalty function approach, *Comput. Meth. Appl. Mech. Eng* **17/18**: 673.

Appendix A

Scaled equations

Upon introducing the dimensionless variables from (2.6) into equations (2.1)-(2.3), the relevant equations for the problem reduce to

$$u_x + w_z = 0, \tag{A1}$$

$$\varepsilon \mathrm{Re}\left(u_t + uu_x + wu_z\right) = -p_x + a\,\mathrm{R}vu_{zz} + \varepsilon^{2-\alpha} q_x + \varepsilon^{1-\beta} s_z + G_L, \tag{A2}$$

$$p_z = \varepsilon^{2-\gamma}\, r_z + \varepsilon^{3-\beta}\, s_x, \tag{A3}$$

$$\mathrm{De}_L\left[\varepsilon^{-\alpha}\left(q_t + uq_x + wq_z - 2qu_x\right) - \; 2\varepsilon^{-1-\beta} s u_z\right] + \varepsilon^{-\alpha} q = a u_x, \tag{A4}$$

$$\mathrm{De}_L\left[\varepsilon^{-\gamma}\left(r_t + wr_z + ur_x - 2rw_z\right) - 2\varepsilon^{1-\beta} s w_x\right] + \varepsilon^{-\gamma} r = 2a\, w_z, \tag{A5}$$

$$\mathrm{De}_L\left[\varepsilon^{-\beta}\left(s_t + uw_x + ws_z\right) - \varepsilon^{-1-\gamma} r u_z - \varepsilon^{1-\alpha} q w_x\right] + \varepsilon^{-\beta} s = a\,\varepsilon^{-1} u_z. \tag{A6}$$

Appendix B

Integrals

$$E0_i = \left\langle \left(1-\xi^2\right) A_i \right\rangle \qquad E1_{ij} = \left\langle \xi A_i A_j' \right\rangle$$

$$E2_{ijk} = \left\langle \phi_k A_j' A_i \right\rangle \qquad E3_{ijk} = \left\langle A_i A_j A_k \right\rangle$$

$$E4_{ij} = \left\langle A_j'' A_i \right\rangle \qquad E5_{ij} = \left\langle A_i D_j' \right\rangle$$

$$E6_{ij} = \left\langle \xi A_i B_j' \right\rangle \qquad E7_{ij} = \left\langle A_i B_j \right\rangle$$

$$E8_i = \left\langle A_i \right\rangle$$

$$F0_i = \left\langle \xi^2 B_i \right\rangle \qquad F1_{ij} = \left\langle \xi B_i B_j' \right\rangle$$

$$F2_{ijk} = \left\langle \phi_k B_i B_j' \right\rangle \qquad F3_{ijk} = \left\langle B_i A_j B_k \right\rangle$$

$$F4_{ijk} = \left\langle \xi A_j' B_i B_k \right\rangle \qquad F5_{ijk} = \left\langle A_j' D_k B_i \right\rangle$$

$$F6_{ijk} = \left\langle A_k B_i B_j \right\rangle$$

$$G1_{ij} = \left\langle \xi C_i C_j' \right\rangle \qquad G2_{ijk} = \left\langle \phi_k C_i C_j' \right\rangle$$

$$G3_{ijk} = \left\langle C_i A_j C_k \right\rangle \qquad G4_{ijk} = \left\langle \xi\left(\xi A_k' + A_k - \phi_k'\right) C_i D_j \right\rangle$$

$$G5_{ijk} = \left\langle \xi \phi_k' D_j C_i \right\rangle \qquad G6_{ijk} = \left\langle \left(\xi A_k - \phi_k\right) D_j C_i \right\rangle$$

$$G7_{ijk} = \left\langle \phi_k D_j C_i \right\rangle \qquad G8_{ijk} = \left\langle \left(\xi A_k' + A_k - \phi_k'\right) C_j C_i \right\rangle$$

$$G9_{ijk} = \left\langle \phi_k' C_j C_i \right\rangle \qquad G10_{ij} = \left\langle \left(\xi A_j' + A_j - \phi_j'\right) C_i \right\rangle$$

$$G11_{ij} = \left\langle \phi_j' C_i \right\rangle$$

$$H0_i = \left\langle \xi D_i \right\rangle \qquad H1_{ij} = \left\langle \xi D_i D_j' \right\rangle$$

$$H2_{ijk} = \left\langle \phi_k D_i D_j' \right\rangle \qquad H3_{ijk} = \left\langle D_i A_j D_k \right\rangle$$

$$H4_{ijk} = \left\langle \xi\left(\xi A_k' + A_k - \phi_k'\right) D_i B_j \right\rangle \qquad H5_{ijk} = \left\langle \xi \phi_k' B_j D_i \right\rangle$$

$$H6_{ijk} = \left\langle \left(\xi A_k - \phi_k\right) B_j D_i \right\rangle \qquad H7_{ijk} = \left\langle \phi_k B_j D_i \right\rangle$$

$$H8_{ijk} = \left\langle A_j' C_k D_i \right\rangle \qquad H9_{ij} = \left\langle A_j' D_i \right\rangle$$